nature cell biology

Mechanical control of the sense of touch by β-spectrin

Michael Krieg[1,2], Alexander R. Dunn[2] and Miriam B. Goodman[1,3]

The ability to sense and respond to mechanical stimuli emanates from sensory neurons and is shared by most, if not all, animals. Exactly how such neurons receive and distribute mechanical signals during touch sensation remains mysterious. Here, we show that sensation of mechanical forces depends on a continuous, pre-stressed spectrin cytoskeleton inside neurons. Mutations in the tetramerization domain of *Caenorhabditis elegans* β-spectrin (UNC-70), an actin-membrane crosslinker, cause defects in sensory neuron morphology under compressive stress in moving animals. Through atomic force spectroscopy experiments on isolated neurons, *in vivo* laser axotomy and fluorescence resonance energy transfer imaging to measure force across single cells and molecules, we show that spectrin is held under constitutive tension in living animals, which contributes to elevated pre-stress in touch receptor neurons. Genetic manipulations that decrease such spectrin-dependent tension also selectively impair touch sensation, suggesting that such pre-tension is essential for efficient responses to external mechanical stimuli.

Owing to their location within skin, muscles, joints and other organs, the sensory neurons responsible for touch, pain and proprioception are continually compressed and stretched. To function properly throughout life, these neurons must therefore resist mechanical stress while retaining sensitivity to minute mechanical stimuli. Cells, including neurons, can be stretched slowly without inducing lasting damage. This structural resilience is believed to depend on a membrane-associated cytoskeleton, but little is known at present about the relevant structures or their mechanical properties within neurons *in vivo*. We sought to fill this knowledge gap and investigate how cell mechanics controls touch sensation.

In *Caenorhabditis elegans*, specialized touch receptor neurons (TRNs) are required for sensation of gentle body touch. Physiological studies[1,2] demonstrate that touch evokes electrical signals in the TRNs and that such responses trigger a simple escape behaviour. The TRNs are well characterized at the molecular and ultrastructural levels[3,4], offering a simple system for investigating how mechanical forces govern cell shape and animal behaviour. Three anterior (ALML, ALMR and AVM) and three posterior TRNs (PLML, PLMR and PVM) tile the body surface, and each is surrounded by a specialized extracellular matrix and the hypodermal cell[4]. Their non-arborized dendrites are filled with a crosslinked bundle of 15-protofilament microtubules and are approximately 500 μm long and 250 nm wide in adult hermaphrodites[4]. They are closer to the body surface than most neurons and are positioned within 200 nm of the skin or cuticle[3,4]. Owing to their anatomical location, TRNs could experience significant mechanical strain not only during body touch but also during locomotion, during which the *C. elegans* propel themselves forward using rhythmic dorsoventral contractions.

Here, we investigate the role played by β-spectrin in neuronal cell mechanics and touch sensation, using AVM and ALM as models. To relate mechanics to function, we provide evidence from single-cell force spectroscopy and *in vivo* laser axotomy that individual TRNs are under constitutive mechanical tension. We further show that spectrin is required for neuronal pre-stress and is likely to be under tensile load, as revealed by fluorescence resonance energy transfer (FRET) probes that detect piconewton forces[5]. We speculate that tension is important for transmission of mechanical force within TRNs, and show that disrupting the spectrin cytoskeleton reduces sensitivity to external touch.

RESULTS

TRNs are subjected to strain in moving animals

To study how neurons react to mechanical deformations, we monitored AVM shape in crawling worms (Fig. 1a and Supplementary Movie 1). The AVM cell closely follows the body's contour in wild-type animals, shortening during ventral bending and elongating during dorsal bending (Fig. 1b,c), similar to a spring under compressive and tensile forces. These observations imply that AVM experiences compressive stress during ventral bending and tensile stress during dorsal bending, and that the cyclical strains generated during crawling produce little physical damage. Thus, wild-type TRNs are both flexible and resistant to mechanical stress. However, the origin of these properties is not fully understood.

[1]Department of Molecular and Cellular Physiology, Stanford University, Stanford, California 94305, USA. [2]Department of Chemical Engineering, Stanford University, Stanford, California 94305, USA.
[3]Correspondence should be addressed to M.B.G. (e-mail: mbgoodman@stanford.edu)

Received 07 July 2013; accepted 10 January 2014; published online 23 February 2014; DOI: 10.1038/ncb2915

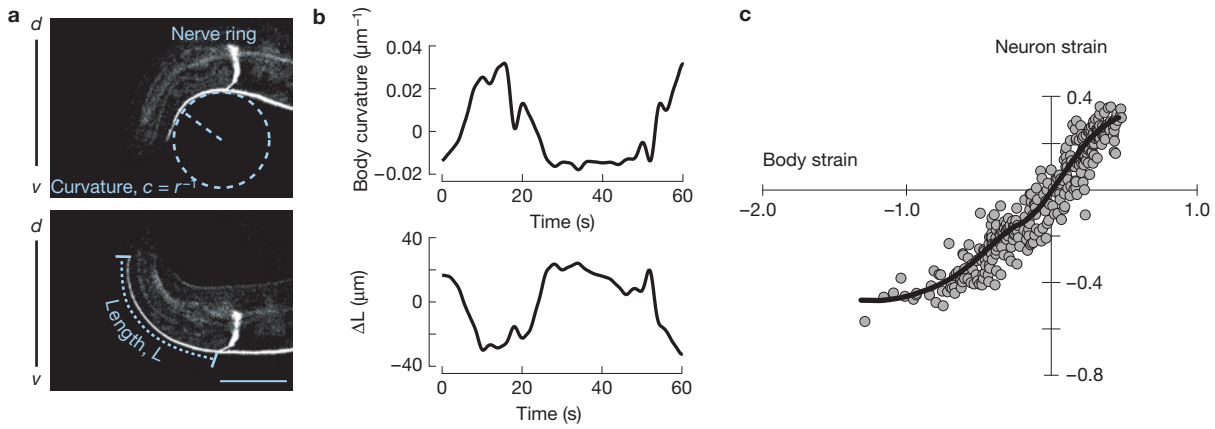

Figure 1 The shape of the AVM sensory neuron during body movement. (**a**) Representative micrographs of a green fluorescent protein (GFP)-labelled AVM neuron in an adult worm bending ventrally (top) or dorsally (bottom). Curvature and neuron length are schematically indicated as dashed lines. Scale bar, 50 μm. (**b**) Body curvature (top) and change in neuron length (bottom) versus time. Epochs of ventral bending correspond to positive curvature and AVM shortening, whereas epochs of dorsal bending correspond to negative curvature and AVM extension. (**c**) Estimated neuron strain, $\Delta L/L$, as a function of body strain. Body strain was derived by approximation of the worm as an Euler–Bernoulli tube, as described in Supplementary Note 1. The black line is a smoothed version of the neuron strain–body strain relationship. Data drawn from $n = 7$ control, TRN::GFP transgenic worms and 352 still images collected during $n = 4$ imaging sessions.

Spectrin is needed for TRN stabilization

In red blood cells, mechanical resilience has long been attributed to a membrane-subjacent, actin–spectrin cytoskeletal network[6–11], and mutations that interfere with network formation cause severe anaemia[7]. In the nervous system, spectrin assembles with actin to form cylindrical networks[12] and spectrin mutations cause motor and cognitive disorders[13]. β-spectrin has 17 spectrin repeats flanked by actin-binding and pleckstrin homology domains and forms α/β-spectrin heterodimers through tetramerization domains in β-spectrin repeat 17 and α-spectrin repeat 0 (ref. 14). Spectrin proteins are conserved in all eukaryotes from protozoa to humans[15] (Supplementary Fig. 1). In *C. elegans*, *unc-70* is the only β-spectrin gene[16,17] and is abundantly expressed in neurons.

As loss of UNC-70 β-spectrin causes movement-induced fractures in motor neurons[18], we reasoned that it might protect TRNs from the mechanical stresses imposed during locomotion. Consistent with this idea, we found that AVM collapses into striking undulations during ventral bending (compressive stress, $\varepsilon < 0$) that straighten during dorsal bending (tensile stress, $\varepsilon > 0$) in *unc-70(s1502)* null mutants (Fig. 2a and Supplementary Movie 2). We quantified this buckling phenotype by plotting local AVM curvature against body curvature (Fig. 2b). In wild-type animals, neuron and body curvature were linearly related and tightly correlated under both tensile and compressive stress ($r = 0.94$). In contrast, loss of *unc-70* function increased the variance in neuron curvature and significantly decreased its correlation with body curvature under compressive, but not tensile stress ($r = 0.6$; $P = 1 \times 10^{-13}$). This analysis also shows that the largest neuronal deformations were seen at the highest body bends. These findings extend previous observations that UNC-70 β-spectrin is essential to maintain neuronal integrity in moving worms[18].

We sequenced the entire *unc-70* locus in two mutants, *unc-70(e524)* and *unc-70(n493)*, and discovered that these alleles encode E2008K and L2044P, respectively. Both missense mutations affect highly conserved residues in spectrin repeat 17 (Supplementary Fig. 1), which is critical for tetramerization and network formation[7,14,19,20]. As the buckling phenotype was similar in missense and null alleles of *unc-70* (Fig. 2), these data point towards an important yet unrecognized role for the spectrin tetramerization domain in the mechanoprotection of neurons in living animals.

In principle, the undulations present in spectrin mutants could reflect a defect in attachment between the AVM and the hypodermis (the epidermis in *C. elegans*) or cuticle. We reasoned that, if detachment were the primary cause of the morphological defects in *unc-70* mutant TRNs, then TRNs would buckle in *him-4* hemicentin mutants in which the neurite is detached from the surrounding hypodermal cell owing to a lack of functional hemidesmosomes[21]. No buckling was evident in *him-4* mutant animals (Supplementary Fig. 2a, b). We furthermore examined the effect of loss of *unc-70* function on the spatial distribution of hemidesmosomes, which occur at regular intervals along the length of the AVM neurite. These structures had a similar organization in *unc-70* and wild-type TRNs (Supplementary Fig. 2c–i)[21,22]. Thus, neuron detachment from the hypodermis does not explain the buckling observed under compressive stresses. As β-spectrin is also present in the hypodermis[16,17] that surrounds the TRNs, the buckling instability found in *unc-70* mutant neurons could reflect a loss of spectrin function in the hypodermis. To test for this possibility, we examined transgenic *unc-70* mutants expressing wild-type UNC-70 only in hypodermis. We found that this manipulation decreased, but did not eliminate, the buckling phenotype (Supplementary Fig. 3a, c). Next, we asked whether disrupting spectrin networks only in the TRNs could phenocopy the effect of *unc-70* loss of function on neuronal morphology. To do this, we reasoned that overexpressing the tetramerization domain of α-spectrin (repeat 0 and 1) selectively in the TRNs would interfere with spectrin network assembly and act similarly to a dominant-negative mutation. Consistent with this idea, the AVM neurons in these TRN::SPC-1(dn) transgenics showed

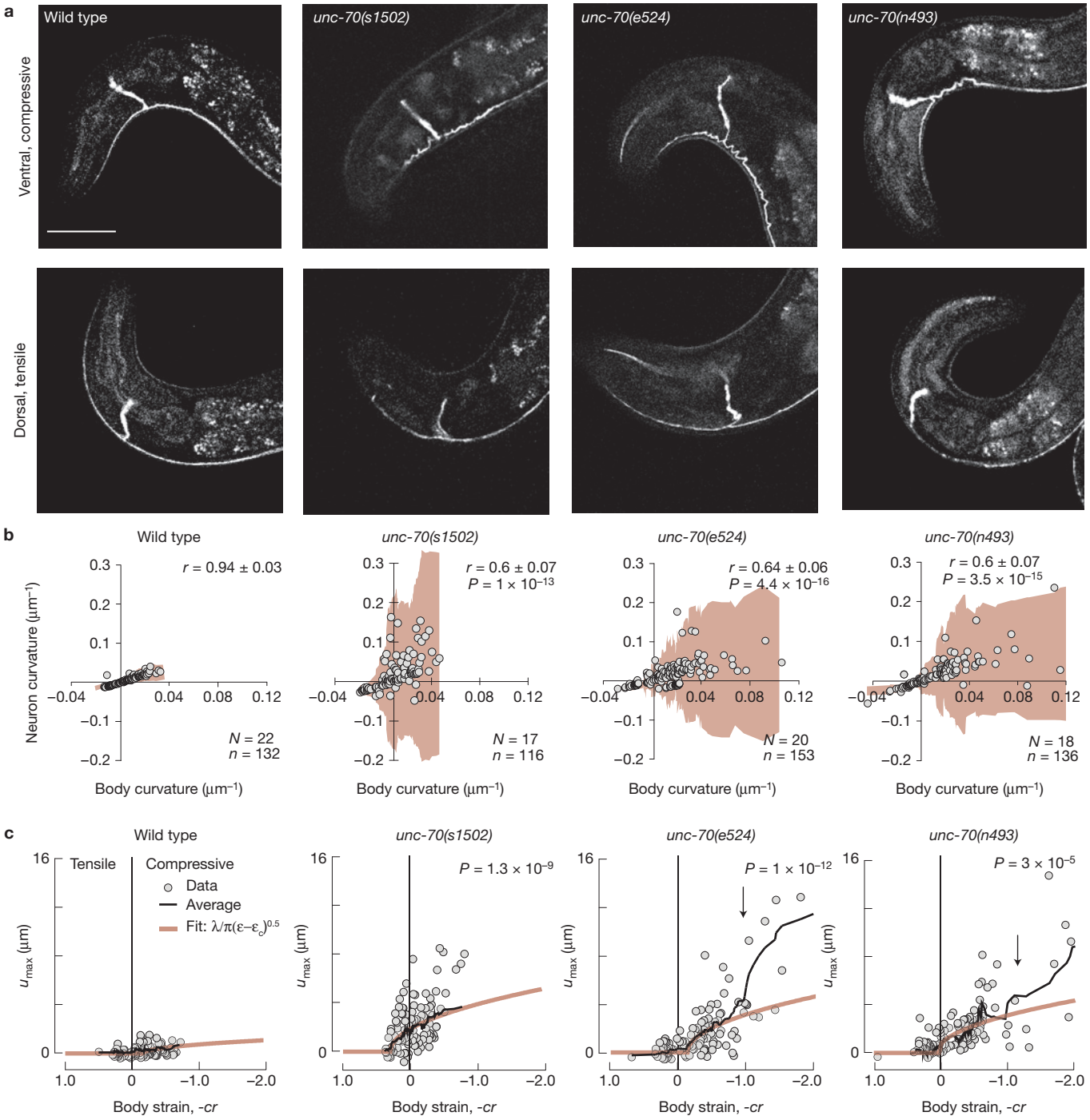

Figure 2 Loss of *unc-70* β-spectrin function causes buckling in TRNs during ventral bending. (**a**) AVM shape during ventral (top) and dorsal (bottom) bending in wild-type and *unc-70* mutant TRN::GFP animals. Scale bar, 50 μm. (**b**) Neuron curvature versus body curvature. Each point is the mean of 10–30 adjacent curvature measurements in a still image (Methods). Shaded areas (beige) indicate the s.d. of neuron curvature; the increased deviation during compressive (positive, ventral) body bends indicates a larger variation in local neuron curvature. *r* values in *unc-70* mutants were significantly different from wild type (Fisher *z*-transform of *r*). *P* values indicated in the upper right. *N*, number of animals; *n*, number of still images. The data are from $n = 3$ imaging sessions. (**c**) u_{max} of AVM as a function of body strain, computed from the product of body curvature, *c*, and the radius of curvature, *r*. Each point is the maximum deformation within a still image. Black lines are running averages of 15 images; beige lines are the calculated buckling deformation of a constrained, flexible filament bundle as a function of compressive strain ε (Supplementary Note 1). Arrows indicate deviation from the model at high curvature due to cuticle buckling. *P* values derived from linear regression and compared with wild type are indicated in the upper left. Same number of observations as in **b**. All strains carry the *uIs31* transgene encoding TRN::GFP.

compression-induced AVM buckling similar to that observed in *unc-70* mutants (Supplementary Fig. 3b, d).

We propose that the compression-induced undulations in *unc-70* mutants (Fig. 2a and Supplementary Movies 2–4) are analogous to the periodic buckling of an axially compressed flexible beam whose motion is constrained by the surrounding medium[23]. In this model of constraint Euler buckling, undulation amplitude increases with the square root of the applied force once the compression exceeds a critical value[24–26]. Consistent with this model, the buckling amplitude, defined as the maximum off-axis deformation, u_{max}, increased in a nonlinear fashion above a critical value of body strain in *unc-70* mutants (Fig. 2c and Supplementary Note 1). Accordingly, we adapted a model of undulation amplitude and wavelength as a function of the stiffness of the constraining material[23,25,27] and used it to draw inferences about material properties of the neuron and its surrounding tissues. The model links $u_{max}(\varepsilon)$ to the wavelength λ of the undulations and a critical strain ε_c (refs 24,25 and Supplementary Note 1):

$$u_{max}(\varepsilon) = \begin{cases} \frac{\lambda}{\pi}\sqrt{\varepsilon - \varepsilon_c}, & \varepsilon > \varepsilon_c \\ u_0, & \varepsilon < \varepsilon_c \end{cases} \quad (1)$$

where $u_0 = 0$ is the buckling amplitude below the critical buckling strain, ε_c. The buckling wavelength λ is inversely proportional to the elastic modulus of the surrounding material[24–26]. Conversely, the critical buckling strain ε_c is directly proportional to the elasticity and pre-strain within the neurite (Methods), which we anticipate to arise from the cortical spectrin network in our model neuron. Fitting equation 1 to the data (Fig. 2c) enabled us to compare λ among wild-type and *unc-70* mutant alleles, yielding this allelic series: wild-type < *unc-70(e524)* E2008K ≤ *unc-70(n493)* L2044P < *unc-70(s1502)* Q575*stop*. Thus, the effective elasticity of the TRNs and their surroundings is larger in wild-type neurons than in *unc-70* mutants. Consistent with this idea, expressing wild-type UNC-70 protein in the hypodermis of *unc-70* mutant animals reduces buckling amplitude and wavelength, but is not sufficient to reduce buckling to wild-type levels (*unc-70* > *unc-70;*Hypo::UNC-70; Supplementary Fig. 3e). In contrast, TRN-specific interference with network formation after overexpression of TRN::SPC-1(dn) shows that a functional spectrin network is needed for stabilization against compressive forces (Supplementary Fig. 3f). Taken together, these findings establish that UNC-70 β-spectrin has cell autonomous and non-autonomous roles in stabilizing TRNs against crawling-induced forces.

Spectrin-deficient TRNs have altered mechanical properties

The picture emerging from these findings is that β-spectrin protects neurons during compression. To directly investigate the role β-spectrin has in cell mechanics, we measured TRN mechanics with two independent approaches: the first uses an atomic force microscope (AFM) to measure the force required to pull membrane tethers from cells in culture[28,29] and the second uses laser axotomy and high-speed imaging of axonal retraction. We found that the force needed to deform the plasma membrane into a highly curved tether was significantly lower in *unc-70* mutant TRNs for a wide range of extrusion velocities (Fig. 3a–c). To relate the extrusion or tether force, F_t, to cell mechanical properties, we fitted our force–velocity data to a recent model[30], estimated the static force at zero velocity, f_0, and used these values to compute the apparent membrane tension, T_{app}, which is a sum of the membrane–cytoskeleton adhesion energy (W_0) and in-plane membrane tension (T_m; refs 30,31). Importantly, we found T_{app} was ∼10 pN μm^{-1} lower in spectrin mutant TRNs than in wild-type cells (Fig. 3d), suggesting that spectrin acts to increase resistance to membrane deformation. Treating TRNs with latrunculin A or cytochalasin D (Fig. 3e,f) to disrupt dynamic actin networks had little, if any, effect on the static tether force. Taken together, these results show that a functional spectrin network is critical for TRN membrane mechanics and suggest that spectrin may function independently of actin dynamics.

TRNs are under constitutive mechanical tension

Given the difference in T_{app} of 10 pN μm^{-1} and the end-to-end length of spectrin tetramers (100–200 nm; refs 12,32), we can estimate that a tensile force of ∼1 pN would be applied to each tetramer if the spectrin network were the main element responsible for the reduced tension in *unc-70* mutants. This implies that individual molecules are stretched and that the spectrin network supports mechanical pre-stress in TRNs *in vivo*. Such a pre-stressed neuron will retract following laser axotomy (Fig. 4a and Supplementary Fig. 4a) at a rate proportional to the pre-tension[33,34]. In wild-type TRNs, little retraction was detected (Supplementary Fig. 4b,c). This could indicate a lack of pre-stress or that attachments between the TRNs and hypodermis prevent retraction *in vivo*. We tested for this possibility by carrying out axotomies in *him-4* hemicentin mutants that have defects in TRN attachment, but wild-type touch sensitivity[21]. As shown in Fig. 4, TRNs retracted several micrometres in less than 1 s. Thus, TRNs recoil as expected for a neuron under tension. To determine the contribution of β-spectrin to pre-stress, we analysed TRN retraction in *him-4;unc-70* double-mutant animals. Such double-mutant TRNs retracted more slowly and to a lesser extent than *him-4* single mutant neurons (Fig. 4c), indicating that pre-stress is *unc-70* dependent. Retraction distance and strain rate were also impaired in transgenic animals expressing dominant-negative α-spectrin selectively in the TRNs (Fig. 4d), indicating that an intact spectrin network is needed within the TRNs themselves to generate proper longitudinal tension.

In living neurites β-spectrin is under tension

In principle, β-spectrin could be held under tension or assist other proteins to maintain or generate pre-stress. We used TSMod, a genetically encoded molecular force sensor[5], to directly visualize tension within spectrin molecules *in vivo* and to differentiate between these possibilities. TSMod consists of a pair of FRET-enabled fluorescent proteins separated by a 40-residue entropic spring derived from spider silk protein[5], which decreases the distance between the FRET partners in the absence of a tensile force. Accordingly, TSMod FRET is high in the absence of force or whenever the fluorophores are close together, but decreases if the fluorophores are pulled apart (Fig. 5a). Previous analysis of this sensor indicates that it can resolve forces between 1 and 5 pN (ref. 5). Thus, it is well suited to measure the force across spectrin *in vivo*, which we estimated as ∼1 pN in our AFM experiments.

Seeking to maximize mechanosensitivity and to minimize disruption of β-spectrin, we inserted TSMod between the eighth and ninth spectrin repeats of UNC-70 β-spectrin, an interface with high flexibility subjected to force-dependent conformational changes[8]. Next, we expressed this fusion protein from the native *unc-70*

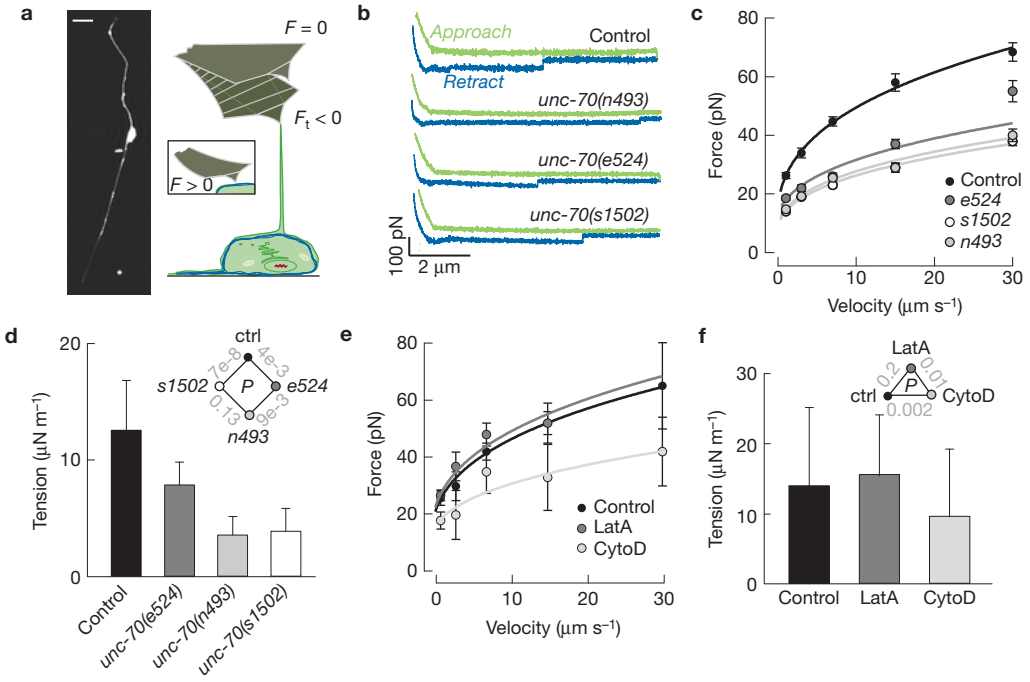

Figure 3 Loss of β-spectrin function decreases TRN tension. (**a**) Micrograph of a GFP-tagged TRN *in vitro* (left) and schematic diagram of the tether extrusion procedure. A peanut lectin-coated AFM cantilever was held in contact with each cell for about 400 ms and a lipid tube formed following retraction in about 20% of cases; such events result in a downward deflection of the cantilever ($F_t < 0$). (**b**) Representative force–distance curves (approach in green, withdrawal in blue) acquired at 7 $\mu m\,s^{-1}$. The discontinuity during retraction indicates an interaction event and is proportional to the membrane tension. Similar results were observed in more than 17 cells per genotype. (**c**) Tether force (mean ± s.e.m.) versus cantilever retraction velocity in control and mutant TRNs. Force–velocity curves were fitted to a power law and used to estimate the static tether force at zero velocity (Methods). Supplementary Table 3 lists the number of cells and tethers for each genotype. Data in **b** and **c** were acquired during $n = 6$ AFM sessions. (**d**) T_{app} of cultured TRNs, derived from the static tether force, f_0, estimated from the fits to the data in **c** according to $T_{app} = f_0^2/(8\pi^2\kappa)$ and a value for the membrane bending rigidity, κ, of 2.7×10^{-19} N m (ref. 29). The diamond inset shows *P* values for the tested combinations. (**e**) Tether force (mean ± s.e.m.) versus cantilever retraction velocity in the presence and absence of drugs that disrupt actin. Latrunculin A (LatA) and cytochalasin D (cytoD) were applied at 1 and 2 µM, respectively. Supplementary Table 3 lists the number of cells and tethers for each condition. Treated and untreated cells were tested in parallel during $n = 3$ AFM sessions. (**f**) Membrane tension is unaffected by actin-depolymerizing drugs. The triangle inset shows *P* values as a function of treatment. *P* values were derived after log–log transformation of the force–velocity data and linear regression followed by a Tukey-type *t*-test. All strains carry the *uIs31* transgene encoding TRN::GFP, which was used to identify TRNs in cultures.

promoter in *unc-70(s1502)* null mutants and tested if the resulting transgene rescued the paralysis seen in *unc-70* mutants, which have an average speed of 7.5 ± 0.8 $\mu m\,s^{-1}$ (mean ± s.e.m., $n = 47$), five times slower than wild-type animals[35]. The average crawling speed of transgenic animals (31 ± 9 $\mu m\,s^{-1}$, mean ± s.e.m., $n = 31$) was both significantly faster ($P = 1 \times 10^{-14}$, Mann–Whitney *U*-test) than *unc-70(s1502)* and comparable to wild-type speeds. UNC-70(TSMod) was expressed broadly in many neurons (Fig. 5b) and, as expected for a protein incorporated into a cytoskeletal network, fluorescence recovery after photobleaching (FRAP) analysis revealed that this protein was significantly less mobile than cytoplasmic TSMod (Supplementary Fig. 5).

Having established that UNC-70(TSMod) mimics the function of the native β-spectrin, we used it to infer stress within neuronal spectrin networks in living animals. We measured FRET by sensitized emission on a pixel-by-pixel calculation (Methods). As both donor and acceptor fluorophores are present within a single protein, the simplest interpretation of differences in FRET efficiency is that they reflect variation in the proximity of the donor to the acceptor. However, FRET could in principle occur between the donor and acceptors present in adjacent molecules. Such intermolecular FRET, if present, is expected to increase with fluorophore concentration. We observed that FRET efficiency was not correlated with acceptor emission (Supplementary Fig. 6a–f), indicating that intermolecular FRET was negligible.

To calibrate our FRET imaging protocol, we replaced the entropic spring in UNC-70(TSMod) with either a stiff linker domain (TRAF) or a short five-residue linker to generate mechanically insensitive, constitutively low- and high-FRET standards (Fig. 5a): UNC-70(TRAF) and UNC-70(5aa) (refs 36–38). We also measured the FRET efficiency of selected TSMod isoforms using fluorescence lifetime imaging microscopy (FLIM) and found similar values for FRET efficiency regardless of whether they were measured with sensitized emission or FLIM (Supplementary Fig. 6g-j). Moreover, FRET values for the constitutive low- and high-FRET standards agree with previously published FRET efficiencies derived from fluorescence lifetime measurements[37,38], enabling us to predict relative distances from our FRET efficiency calculations.

With a robust method to quantify FRET as a function of chromophore separation, we measured neuronal FRET *in vivo*

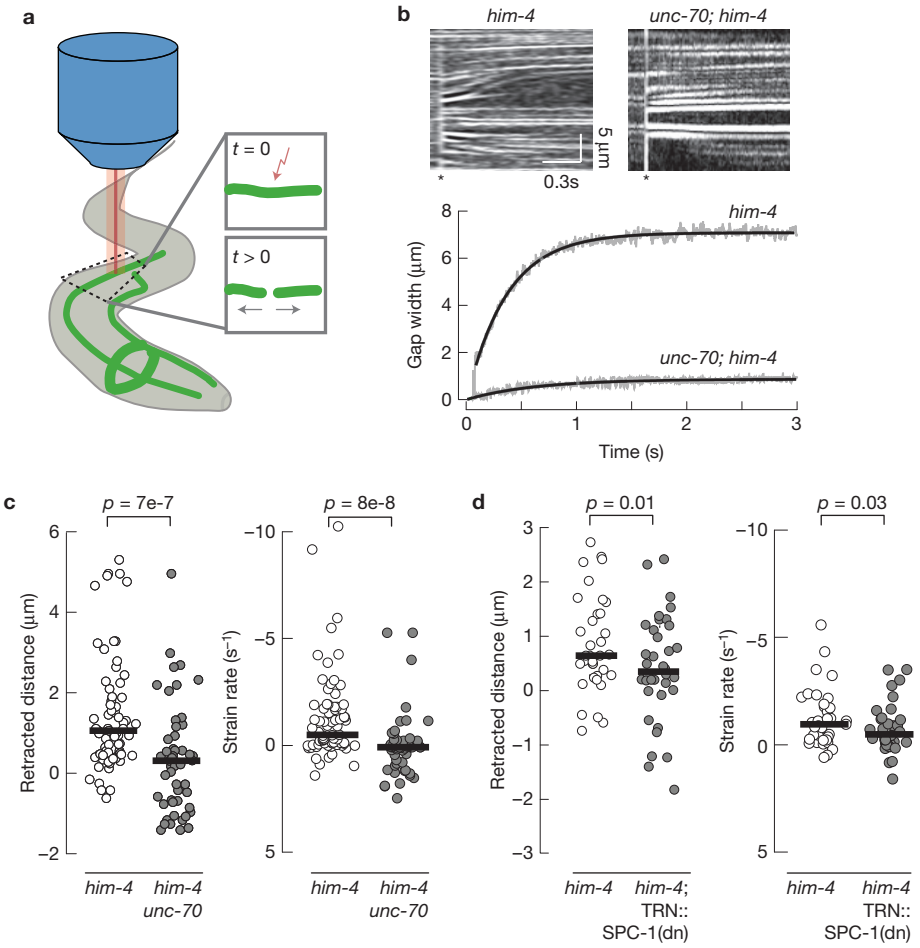

Figure 4 *unc-70(e524)* TRNs fail to retract after laser axotomy. (**a**) Schematic diagram of the laser cutting experiment. One Ti::sapphire laser was used to cut TRN axons in immobilized worms, whereas a second, identical laser was used to simultaneously image the neuron at 1 kHz. (**b**) Representative kymographs of control *him-4(e1267)* (top, left) and mutant *him-4(e1267); unc-70(e524)* (top, right) TRNs before and after axotomy. For visualization, kymographs were processed with a Laplace edge detection algorithm to highlight fluorescent speckles. Retraction is evident from the outward motion of fluorescence speckles. Time runs from left to right. The asterisks indicate the time of ablation. (**c**) Retracted distance (left) and strain rate (right) of control and *unc-70(e524)* mutant TRNs in a *him-4* mutant background after laser cutting. Each point is a single axotomy and thick horizontal bars are the median of 69 and 54 axotomies in 19 control and 22 mutant animals, respectively. Data were collected during $n = 7$ axotomy sessions. Median values were significantly different (*U*-test); *P* values are indicated above. (**d**) Retracted distance, $D_0/2$ (left), and strain rate (right) of control and TRN::SPC-1(dn) TRNs in a *him-4* mutant background after laser cutting. Each point is a single axotomy and thick horizontal bars are the median of 37 and 38 cuts in 16 control and 13 TRN::SPC-1(dn) transgenic animals, respectively. Data in **c** and **d** derived by fitting plots of gap width versus time to $D(t) = D_0(1 - \exp(-\tau t)) + D_a$, where $D(t)$ is the gap width as a function of time, D_0, is the final gap width, and D_a is the initial gap. The retracted distance is given by $D_0/2$ and strain rate by $(D_0/2)(\tau/D_a)$.

(Fig. 5c). The average FRET efficiency of UNC-70(TSMod) in the TRNs was intermediate between the average FRET efficiency values observed for UNC-70(TRAF) and UNC-70(5aa) (Fig. 5c). UNC-70(TSMod) is expressed in other neurons (Fig. 5b) that had FRET efficiency values similar to the TRNs (Fig. 5c). From this result, we infer that mechanical tension is a shared property of spectrin-expressing neurons. To interpret UNC-70(TSMod) FRET values and deduce whether or not UNC-70 is under tension, we generated two constructs in which TSMod is predicted to experience little or no strain: cytoTSMod, a soluble protein in the cytoplasm, and UNC-70(N-TSMod), an amino-terminal fusion that places TSMod in a position where it cannot be stretched. Consistent with the hypothesis that UNC-70 is under tension, the FRET efficiency of UNC-70(TSMod) was significantly lower than that found in either of these two constructs (Fig. 5c). We leveraged a previous TSMod calibration[5] and the FRET efficiency of the UNC-70(TSMod) indicator when compared with soluble TSMod to estimate that individual UNC-70 β-spectrin molecules are loaded to ~1.5 pN. This value is surprisingly close to the estimate obtained from our *in vitro* AFM assay. Thus, not only is β-spectrin required to maintain tension in TRNs, but also the molecule itself is held under steady-state pre-stress in neurons *in vivo*.

Next, we determined how manipulations expected to disrupt the spectrin network affect the signals provided by the UNC-70(TSMod) sensor. First, we exploited TRN::SPC-1(dn) to disrupt the spectrin network selectively in the TRNs. As shown in Fig. 5d, this resulted

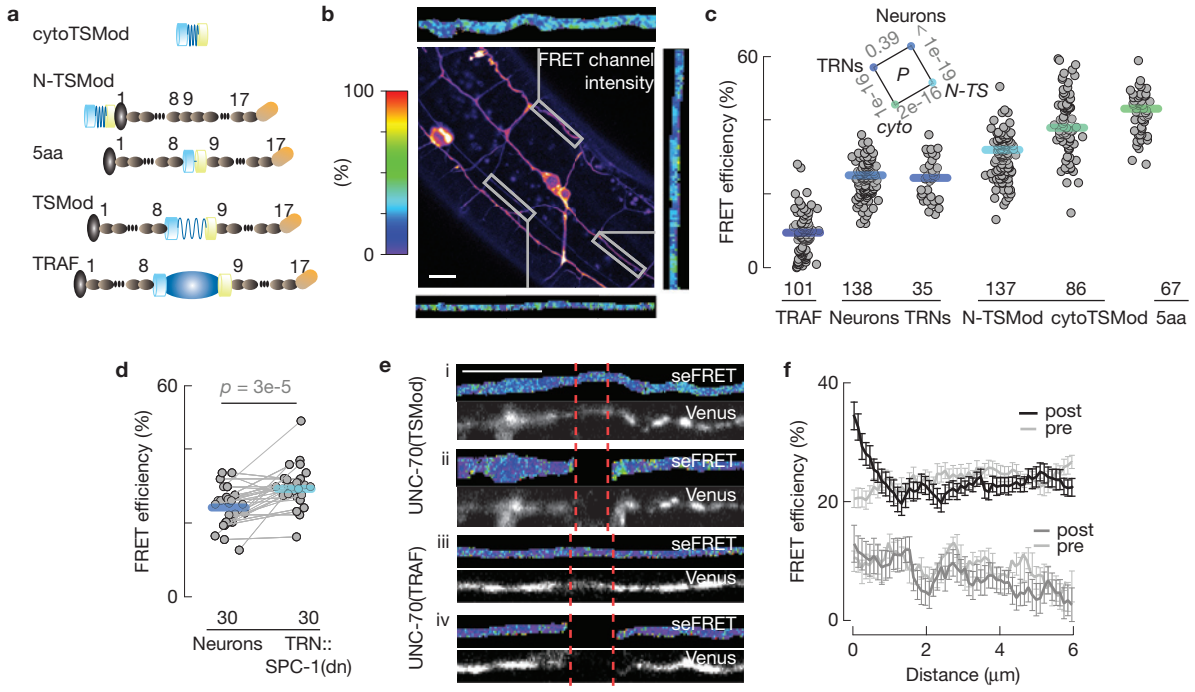

Figure 5 UNC-70 is under constitutive tension in neurons of living animals. (**a**) TSMod–UNC-70 β-spectrin fusion proteins. Shown schematically in descending order of expected FRET efficiency (top to bottom): cytoTSMod, N-TSMod, 5aa, UNC-70(TSMod) and TRAF. Symbols are the following: teal cylinder, monomeric teal fluorescent protein (mTFP); blue spring, spider silk linker; yellow cylinder, Venus; grey oval, UNC-70 actin-binding domain; charcoal oval, spectrin repeats; dark blue oval, TRAF domain. (**b**) Representative confocal microscopy image of the uncorrected FRET channel after mTFP donor excitation and recording the Venus acceptor emission. Scale bar: 10 μm. Flanking the image are images of FRET efficiency for three regions of interest (ROIs). (**c**) FRET efficiency of the TSMod fusion proteins illustrated in **a**. TRNs were identified on the basis of their distinctive morphology and position. CytoTSMod and N-TSMod are no-force controls, whereas UNC-70(TRAF) and UNC-70(5aa) are low- and high-FRET controls. Each point corresponds to the mean FRET efficiency of a single ROI; thick bars are the median values across ROIs; data were collected during eight imaging sessions. Distributions were normal (Jarque–Bera test) and the inset shows *P* values derived from *t*-tests for the indicated combinations. The sample size required to estimate the minimal difference between UNC-70(TSMod) and the no-force controls is 15 at the level of $\alpha = 0.01$. The minimum detectable difference for the presented data is $\delta = 1.7\%$. (**d**) FRET efficiency in TRNs and nearby neurons in TRN::SPC-1(dn) transgenics. Lines connect neuron pairs measured in the same animal. The *P* value (paired *U*-test) is shown above. (**e**) Laser axotomy increases UNC-70(TSMod) FRET adjacent to the cut site. Panels i–iv show representative micrographs of TRNs before (i, iii) and after (ii, iv) axotomy in animals expressing UNC-70(TSMod) (i, ii) or UNC-70(TRAF) (iii, iv). Each pair of micrographs shows the FRET efficiency (top) and acceptor fluorescence (bottom). The colour scale is the same as in **b** and **c**. (**f**) FRET efficiency as a function of distance from the cut site. Points are the mean (±s.e.m.) of 23 and 17 axotomies for each UNC-70(TSMod) and UNC-70(TRAF), respectively. Neurites were imaged at the same position before axotomy (grey traces, 'pre'). As expected for an axotomy-induced tension release, FRET was highest near the cut site and declined to control values within 2 μm. Data were collected during $n = 3$ imaging sessions.

in higher FRET efficiency (decreased tension) in the TRNs when compared with other neurites in the same animals. Second, we tested whether laser axotomy could release tension within the spectrin network. We found that UNC-70(TSMod) FRET efficiency increased near the cut site and decreased with distance (Fig. 5e,f). The localized increase in FRET (decreased tension) is specific to the force-sensing fusion protein, because we see that no such increase was detected in UNC-70(TRAF) transgenics (Fig. 5f). Collectively, these data show that individual β-spectrin molecules are under constitutive tension in living neurons and contribute to axonal pre-stress.

Loss of spectrin network function impairs touch sensitivity, but not TRN signalling

Other functions important for mechanoreceptor function could include mechanical signal transmission via a pre-stressed cytoskeleton[39]. If a pre-stressed spectrin network serves this function, then manipulations that decrease TRN tension should also compromise touch sensitivity. To investigate this possibility, we quantified the touch sensitivity by scoring avoidance responses evoked by stroking individual animals with an eyebrow hair[40] (Fig. 6a). In ten-trial assays, wild-type animals responded significantly better than spectrin mutants (Fig. 6a–c), indicating that touch sensitivity was decreased, but not eliminated, in spectrin loss of function genotypes. We also tested the influence of spectrin expression in the hypodermis in *unc-70(e524)* and *unc-70(n493)* mutants. Whereas the hypodermal rescue reduced compression-induced buckling (Supplementary Fig. 3), it had no apparent effect on the touch response in *unc-70* mutants, a result that suggests that the touch defect is due to loss of spectrin-dependent tension in the TRNs themselves. Consistent with this idea, the expression of a dominant negative α-spectrin, SPC-1(dn), in the TRNs was sufficient to decrease touch sensitivity (Fig. 6d). Taken together, these data suggest that β-spectrin acts inside the TRNs to increase sensitivity to gentle touch and that proper mechanical tension is essential for mechanosensitivity.

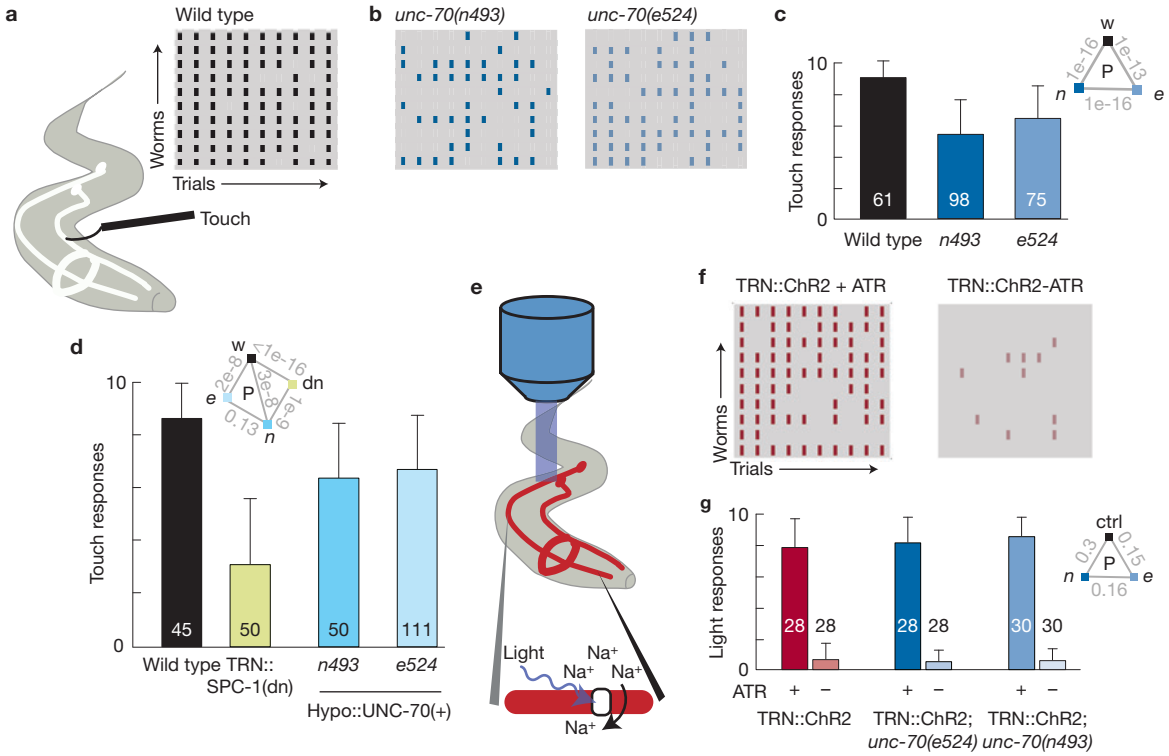

Figure 6 Loss of *unc-70* function impairs touch sensitivity, but not synthetic light sensitivity. (**a**–**d**) Touch response in wild-type and *unc-70* mutants. (**a**) Schematic diagram of the assay used to measure touch sensitivity and ethogram of touch responses in wild type (N2). Rows represent individual worms, columns are trials and black ticks indicate a stimulus-evoked reversal. (**b**) Ethogram of *unc-70(n493)* and *unc-70(e524)* mutant animals. (**c**) Average touch response as a function of genotype. Bars are mean ± s.d., numbers on each bar show the number of animals tested blind to genotype during $n = 4$ assay sessions; the inset shows *P* values derived from a *U*-test. (**d**) Average response rate in transgenic animals with TRN-specific defects in spectrin function or hypodermis-specific expression of wild-type UNC-70. Bars are mean ± SD, numbers on each bar show the number of animals tested blind to genotype during $n = 2$ or $n = 4$ assay sessions for TRN::SPC-1(dn) and *unc-70;* HYPO::UNC-70(+) transgenics, respectively; the inset shows *P* values derived from a *U*-test. (**e**–**g**) Light-induced reversal in transgenic animals expressing ChR2 selectively in the TRNs (TRN::ChR2). (**e**) Schematic diagram of optogenetic stimulation. (**f**) Ethogram of the response of TRN::ChR2 control animals to blue light in the presence (left) and absence (right) of all-*trans* retinal (ATR). (**g**) Average light response in control and *unc-70* mutants grown in the presence (green, blue bars) or absence (grey bars) of ATR and stimulated with brief (1 s) light pulses of 0.48 mW mm^{-2}. Bars are mean ± SD, the number of animals tested during $n = 2$ assay sessions is indicated near each bar; the inset shows *P* values derived from a Mann–Whitney *U*-test.

Spectrin-dependent pre-stress could enhance the ability of the TRNs to detect touch or have a more general role in TRN physiology, including synaptic transmission[41]. To differentiate between these possibilities, we obtained transgenic animals expressing channelrhodopsin-2 in the TRNs (TRN::ChR2)[42]. In these animals, TRNs can be activated either mechanically or optically. Consistent with previous studies[42,43], only TRN::ChR2 animals grown with all-trans retinal (ATR), which is necessary for ChR2 function, reversed direction in response to blue light (Fig. 6e–g). We also found that *unc-70* mutants have wild-type responses to light, but impaired touch sensation. From these data, we infer that loss of β-spectrin function has no detectable effect on TRN physiology or neurotransmission, but that β-spectrin enhances sensitivity to touch by regulating mechanical signal transmission.

DISCUSSION

We combined genetic dissection with *in vivo* and *in vitro* analysis of neuronal cell mechanics to show that UNC-70 β-spectrin is needed to protect them from mechanical stress. Several lines of evidence support the conclusion that TRNs are held under mechanical pre-stress and that the tension is partially borne by a spectrin network. First, *unc-70* mutant AVM neurons buckle in response to compressive stress during movement. Second, we show that an intact spectrin network is essential to maintain tension in the TRNs. Third, FRET measurements with UNC-70(TSMod) establish that spectrin is itself under tension. Importantly, such tension can be decreased by both physical and genetic disruption of the spectrin network in the TRNs. Using genetic and optogenetic dissection, we also show that disrupting the TRN spectrin network impairs touch sensation and leaves synthetic light-activated behaviours intact, a result that suggests that spectrin is needed for mechanical activation of the TRNs, but not for downstream signalling in the TRNs or in the neural circuit linking their activation to behavioural responses. Together, these findings show that spectrin contributes to at least two functions in sensory neurons—mechanoprotection and touch sensation.

How might TRNs make use of a mechanically pre-stressed spectrin network? Both the hypodermal and neuronal spectrin networks help to protect neurons from mechanical stress and suppress buckling

instabilities. By increasing the pre-tension in the neuron, buckling will not occur until the tension is eliminated by the compressive stress, thus providing an effective mechanism for mechanoprotection. The restoring force after a transverse deformation due to a point load is a sum of the pre-stress and elastic contributions[44]. In the limit of small deformations, the elasticity term has little contribution to the total restoring force owing to the negligible flexural rigidity of the neuron. Hence, proper spectrin network formation potentially ensures a restoring force and acts as a strain buffer to protect the neuron from damage during touch and locomotion. If the compressive force, however, exceeds the critical limit and buckling occurs, lateral movement of the neuron will unavoidably deform surrounding tissues. Hence, a higher elasticity of the surrounding hypodermal cell will provide a larger lateral constraint and minimize buckling. Without this further stabilization, the neuron will undergo significant buckling, as seen in animals lacking both neuronal and hypodermal spectrin networks.

Force transmission has been implicated in several systems involving signal transduction via actin stress fibres[39], during phototransduction in the fly retina[45] and sensory mechanotransduction in vertebrate hair cells[46]. Notably, mechanical stimulation during touch in *C. elegans* can activate 20–30 MeT channels within milliseconds[1]. Such channels localize to puncta separated by about 2–4 μm (ref. 4), suggesting that signals are transmitted over a distance of the order of 100 μm in a few milliseconds. As pre-stress is known to modulate the transmission speed of mechanical signals in viscoelastic media[44,47], we propose that spectrin-dependent tension may govern rapid channel activation and tune sensitivity to applied stresses. Further work will be needed to discover whether such transmission occurs primarily by direct connections between spectrin and MeT channels or through spectrin-guided mechanical signal transmission in the plasma membrane.

As spectrin is a ubiquitous component of the neuronal cytoskeleton from worms to humans, and has recently been shown to form a cylindrical network in neurons[12], we hypothesize that pre-stress is an emergent property of the cortical cytoskeleton in neurons that helps to protect neurons from damage and may also serve as a molecular stress distributor in sensory neurons embedded in our skin, muscles, joints and internal organs. □

ACKNOWLEDGEMENTS

We thank J. Shaw, A. Slade and S. Minne of Bruker Instruments for generous loan of AFM; Z. Liao for worm injections; D. Ramallo, C. Buckley, A. Olson, J. Mulholland for assistance with microscopy; K. Shen for loan of equipment for worm injection and strain integration; C.P. Heisenberg, K.C. Huang and W.J. Nelson for comments. Confocal microscopy and laser axotomy conducted in the Neuroscience Microscopy Service (NMS, partially supported by NS06973) and the Cell Science Imaging Facility (CSIF) at Stanford. Some strains provided by M. Chalfie, E. Jorgensen, W. Schaefer and the Caenorhabditis Genetics Center, which is funded by the NIH Office of Research Infrastructure Programs (partially supported by S10RR05574). Work supported by a Stanford Bio-X IIP award (A.R.D., M.B.G.), the National Institutes of Health (DP2OD007078 to A.R.D., RO1NS047715 and RO1EB006745 to M.B.G.), the National Science Foundation (No. 1136790, A.R.D.), Stanford Cardiovascular Institute Seed Grant (A.R.D.), Burroughs-Wellcome Career Award at the Scientific Interface (A.R.D.) and a Long-term fellowship from HFSP (M.K.).

AUTHOR CONTRIBUTIONS

M.K., A.R.D. and M.B.G. conceived the research and designed experiments; M.K. carried out and analysed experiments; M.K., A.R.D. and M.B.G. wrote the paper.

COMPETING FINANCIAL INTERESTS

The authors declare no competing financial interests.

Published online at www.nature.com/doifinder/10.1038/ncb2915
Reprints and permissions information is available online at www.nature.com/reprints

1. O'Hagan, R., Chalfie, M. & Goodman, M. B. The MEC-4 DEG/ENaC channel of *Caenorhabditis elegans* touch receptor neurons transduces mechanical signals. *Nat. Neurosci.* **8,** 43–50 (2005).
2. Suzuki, H. *et al. In vivo* imaging of *C. elegans* mechanosensory neurons demonstrates a specific role for the MEC-4 channel in the process of gentle touch sensation. *Neuron* **39,** 1005–1017 (2003).
3. Chalfie, M. & Thomson, J. N. Structural and functional diversity in the neuronal microtubules of *Caenorhabditis elegans*. *J. Cell Biol.* **93,** 15–23 (1982).
4. Cueva, J. G., Mulholland, A. & Goodman, M. B. Nanoscale organization of the MEC-4 DEG/ENaC sensory mechanotransduction channel in *Caenorhabditis elegans* touch receptor neurons. *J. Neurosci.* **27,** 14089–14098 (2007).
5. Grashoff, C. *et al.* Measuring mechanical tension across vinculin reveals regulation of focal adhesion dynamics. *Nature* **466,** 263–266 (2010).
6. Bennett, V. & Baines, A. J. Spectrin and ankyrin-based pathways: metazoan inventions for integrating cells into tissues. *Physiol. Rev.* **81,** 1353–1392 (2001).
7. Gaetani, M., Mootien, S., Harper, S., Gallagher, P. G. & Speicher, D. W. Structural and functional effects of hereditary hemolytic anemia-associated point mutations in the alpha spectrin tetramer site. *Blood* **111,** 5712–5720 (2008).
8. Johnson, C. P., Tang, H.-Y., Carag, C., Speicher, D. W. & Discher, D. E. Forced unfolding of proteins within cells. *Science* **317,** 663–666 (2007).
9. Liu, S. C. & Palek, J. Spectrin tetramer-dimer equilibrium and the stability of erythrocyte membrane skeletons. *Nature* **285,** 586–588 (1980).
10. Sleep, J., Wilson, D., Simmons, R. & Gratzer, W. Elasticity of the red cell membrane and its relation to hemolytic disorders: an optical tweezers study. *Biophys. J.* **77,** 3085–3095 (1999).
11. Waugh, R. E. & Agre, P. Reductions of erythrocyte membrane viscoelastic coefficients reflect spectrin deficiencies in hereditary spherocytosis. *J. Clin. Invest.* **81,** 133–141 (1988).
12. Xu, K., Zhong, G. & Zhuang, X. Actin, spectrin, and associated proteins form a periodic cytoskeletal structure in axons. *Science* **339,** 452–456 (2013).
13. Ikeda, Y. *et al.* Spectrin mutations cause spinocerebellar ataxia type 5. *Nat. Genet.* **38,** 184–190 (2006).
14. Li, D. *et al.* A comprehensive model of the spectrin divalent tetramer binding region deduced using homology modeling and chemical cross-linking of a mini-spectrin. *J. Biol. Chem.* **285,** 29535–29545 (2010).
15. Baines, A. J. Evolution of spectrin function in cytoskeletal and membrane networks. *Biochem. Soc. Trans.* **37,** 796–803 (2009).
16. Hammarlund, M., Davis, W. S. & Jorgensen, E. M. Mutations in beta-spectrin disrupt axon outgrowth and sarcomere structure. *J. Cell Biol.* **149,** 931–942 (2000).
17. Moorthy, S., Chen, L. & Bennett, V. *Caenorhabditis elegans* beta-G spectrin is dispensable for establishment of epithelial polarity, but essential for muscular and neuronal function. *J. Cell Biol.* **149,** 915–930 (2000).
18. Hammarlund, M., Jorgensen, E. M. & Bastiani, M. J. Axons break in animals lacking α-spectrin. *J. Cell Biol.* **176,** 269–275 (2007).
19. Bignone, P. A. & Baines, A. J. Spectrin alpha II and beta II isoforms interact with high affinity at the tetramerization site. *Biochem. J.* **374,** 613–624 (2003).
20. Ipsaro, J. J. *et al.* Crystal structure and functional interpretation of the erythrocyte spectrin tetramerization domain complex. *Blood* **115,** 4843–4852 (2010).
21. Vogel, B. E. & Hedgecock, E. M. Hemicentin, a conserved extracellular member of the immunoglobulin superfamily, organizes epithelial and other cell attachments into oriented line-shaped junctions. *Development* **128,** 883–894 (2001).
22. Hresko, M. C., Schriefer, L. A., Shrimankar, P. & Waterston, R. H. Myotactin, a novel hypodermal protein involved in muscle-cell adhesion in *Caenorhabditis elegans*. *J. Cell Biol.* **146,** 659–672 (1999).
23. Landau, L. D., Pitaevskii, L. P., Lifshitz, E. M. & Kosevich, A. M. *Theory of Elasticity, 3rd ed vol. 7* (Butterworth-Heinemann, , 1986).
24. Jiang, H. & Zhang, J. Mechanics of microtubule buckling supported by cytoplasm. *J. Appl. Mech.* **75,** 061019-1 to 061019-9 (2008).
25. Xiao, J. *et al.* Mechanics of buckled carbon nanotubes on elastomeric substrates. *J. Appl. Phys.* **104,** 033543–033543 (2008).
26. Xiao, J. *et al.* Mechanics of nanowire/nanotube in-surface buckling on elastomeric substrates. *Nanotechnology* **21,** 085708 (2010).
27. Brangwynne, C. P. *et al.* Microtubules can bear enhanced compressive loads in living cells because of lateral reinforcement. *J. Cell Biol.* **173,** 733–741 (2006).
28. Diz-Muñoz, A. *et al.* Control of directed cell migration in vivo by membrane-to-cortex attachment. *PLoS Biol.* **8,** e1000544 (2010).
29. Hochmuth, F. M., Shao, J. Y., Dai, J. & Sheetz, M. P. Deformation and flow of membrane into tethers extracted from neuronal growth cones. *Biophys. J.* **70,** 358–369 (1996).
30. Brochard-Wyart, F., Borghi, N., Cuvelier, D. & Nassoy, P. Hydrodynamic narrowing of tubes extruded from cells. *Proc. Nat. Acad. Sci. USA* **103,** 7660–7663 (2006).
31. Sheetz, M. P. Cell control by membrane-cytoskeleton adhesion. *Nat. Rev. Mol. Cell Biol.* **2,** 392–396 (2001).
32. Nans, A., Mohandas, N. & Stokes, D. L. Native ultrastructure of the red cell cytoskeleton by cryo-electron tomography. *Biophys. J.* **101,** 2341–2350 (2011).
33. Kumar, S. *et al.* Viscoelastic retraction of single living stress fibers and its impact on cell shape, cytoskeletal organization, and extracellular matrix mechanics. *Biophys. J.* **90,** 3762–3773 (2006).

34. Ma, X., Lynch, H. E., Scully, P. C. & Hutson, M. S. Probing embryonic tissue mechanics with laser hole drilling. *Phys. Biol.* **6,** 036004 (2009).
35. Ramot, D., Johnson, B. E., Berry, T. L., Carnell, L. & Goodman, M. B. The parallel worm tracker: a platform for measuring average speed and drug-induced paralysis in nematodes. *PloS One* **3,** e2208 (2008).
36. Borghi, N. *et al.* E-cadherin is under constitutive actomyosin-generated tension that is increased at cell-cell contacts upon externally applied stretch. *Proc. Nat. Acad. Sci. USA* **109,** 12568–12573 (2012).
37. Day, R. N., Booker, C. F. & Periasamy, A. Characterization of an improved donor fluorescent protein for Forster resonance energy transfer microscopy. *J. Biomed. Opt.* **13,** 031203 (2008).
38. Koushik, S. V., Chen, H., Thaler, C., Puhl, I. I. I. H. L. & Vogel, S. S. Cerulean, Venus, and VenusY67C FRET reference standards. *Biophys. J.* **91,** L99–L101 (2006).
39. Na, S. *et al.* Rapid signal transduction in living cells is a unique feature of mechanotransduction. *Proc. Nat. Acad. Sci. USA* **105,** 6626–6631 (2008).
40. Hart, Anne C. ed. Behavior (July 3, 2006), *WormBook*, ed. The *C. elegans* Research Community, WormBook, http://dx.doi.org/10.1895/wormbook.1.87.1 .
41. Pielage, J., Fetter, R. D. & Davis, G. W. Presynaptic spectrin is essential for synapse stabilization. *Curr. Biol.* **15,** 918–928 (2005).
42. Schmitt, C., Schultheis, C., Husson, S. J., Liewald, J. F. & Gottschalk, A. Specific expression of channelrhodopsin-2 in single neurons of *Caenorhabditis elegans*. *PloS One* **7,** e43164 (2012).
43. Leifer, A. M., Fang-Yen, C., Gershow, M., Alkema, M. J. & Samuel, A. D. T. Optogenetic manipulation of neural activity in freely moving *Caenorhabditis elegans*. *Nat. Methods* **8,** 147–152 (2011).
44. Hwang, Y. & Barakat, A. I. Dynamics of mechanical signal transmission through prestressed stress fibers. *PloS One* **7,** e35343 (2012).
45. Hardie, R. C. & Franze, K. Photomechanical responses in Drosophila photoreceptors. *Science* **338,** 260–263 (2012).
46. Peng, A. W., Salles, F. T., Pan, B. & Ricci, A. J. Integrating the biophysical and molecular mechanisms of auditory hair cell mechanotransduction. *Nat. Commun.* **2,** 523 (2011).
47. Kuiken, G. D. C. Wave propagation in a thin-walled liquid-filled initially stressed tube. *J. Fluid Mech.* **141,** 289–308 (1984).

METHODS

Strains, genome sequencing and transgenesis. *C. elegans* strains were propagated as described[48] and N2 and TU2769 *uIs31* [Pmec-17::GFP] were used as wild-type controls. A complete list of strains is presented in Supplementary Table 1. All experiments were carried out with L4 or young adult hermaphrodites.

The molecular defect in *unc-70(e524)* and *unc-70(n493)* was determined by sequencing genomic DNA isolated from mixed stage worms (gDNA kit, Qiagen). In brief, the fragment corresponding to the *unc-70* locus was amplified with long-range PCR with the primers MK16 and MK09R (Supplementary Table 2). A 9000 base pair (bp) fragment was isolated and sequenced to reveal a single consistent nucleotide change apparent in each mutant: *unc-70(e524)* encodes G6024A and E2008K, whereas *unc-70(n493)* encodes T6132C and L2044P (Supplementary Fig. 1).

Young adult worms were injected with constructs of interest (25 ng μl^{-1} or 10 ng μl^{-1}) together with a co-transformation marker (Pmyo-3::mCherry, Pmyo-2::mCherry or Punc-122::RFP (red fluorescent protein) at 2–10 ng μl^{-1}) and linearized N2 carrier DNA (50 ng μl^{-1}). At least three lines were subjected to initial analyses; results from a single line are presented for clarity. UNC-70 isoforms were injected into *unc-70(s1502);oxIs95* animals, which harbour a null allele of *unc-70* and an integrated transgene that restores wild-type UNC-70 to the hypodermis[18]. Strains carrying stable arrays were crossed with N2 to create strains carrying the same array in both the *unc-70(s1502)* and N2 backgrounds. Transgenic expression of UNC-70(TSMod) in *unc-70(s1502)* mutants partially rescued locomotion and touch defects. Other transgenics were created in an N2 wild-type background.

Constructs for transgenic expression. *Wild-type UNC-70.* A plasmid encoding wild-type UNC-70 was built as follows. First, RNA was extracted from mixed stage worms (TRIZOL, Ambion RNA isolation kit), eluted in RNAse-free water, and used as a template for PCR with reverse transcription (VILO cDNA kit, Invitrogen), which was conducted in the presence of RNAse inhibitor (Superrase, Ambion). *unc-70* complementary DNA was isolated in two fragments: a 5' 3200-bp fragment was amplified with primers MK16 and MK12R and a 3' 3600-bp fragment was amplified with primers MK13F and MK09R. The two fragments were joined using overlap extension PCR (Phusion polymerase, NEB) and blunt-cloned into a pCR Blunt sequencing vector (Invitrogen). Sequencing this product revealed that it corresponds to the main transcript encoded by *unc-70*, K11C4.3a, which is expressed in adult neurons, hypodermis and muscles[17,18].

The endogenous *unc-70* promoter was isolated from genomic DNA using primer pair MK17, which contains a HindIII site and an SpeI site, and cloned into the pCR Blunt vector to create pCR:Punc-70. Both, pCR:Punc-70 and *unc-70* cDNA were digested with HindIII and SpeI to create pCR:unc70E containing the endogenous promoter fused to the full-length *unc-70* open reading frame. In a last step, the *unc-54* 3′ untranslated region (3′UTR) was inserted into pCR:unc70E and injected into *unc-70(s1502);oxIs95* transgenic animals together with co-transformation marker, Pmyo-3::mCherry. *unc-70(s1502);oxIs95* mutant animals expressing full-length *unc-70* cDNA showed a complete rescue of the uncoordinated (Unc) phenotype associated with *unc-70* (not shown).

UNC-70(TSMod). The tension sensor, TSMod[5], was inserted into UNC-70 between spectrin repeats 8 and 9, following residue 1166. This was accomplished with a four-way Gateway™ recombination strategy. The four entry clones contained (1) *unc-70* promoter, as described above; (2) the N-terminal fragment of *unc-70* (encoding residues 1–1166), (3) TSMod and (4) the carboxy-terminal fragment of *unc-70* (encoding residues 1167–2267) fused to the *unc-54* 3′UTR. The fragments were amplified by PCR using primers 1–8 (Supplementary Table 2) and combined with the appropriate DONR vector in a standard BP reaction, yielding four Entry clones: pENTR Punc-70[1 5], pENTR ATG-R8[5 4], pENTR TSMod[4 3] and pENTR R9-TAA[3 2]. These clones were combined in a standard LR reaction overnight with pDEST14 (Invitrogen), yielding the assembled construct Punc-70::UNC-70(1–1166)::TSMod::UNC-70(1167–2267)::unc-54 3′UTR, which was verified by sequencing.

High FRET (5aa), low FRET (TRAF), cytoTSMod and N-TSMod. Constitutively high-FRET and low-FRET constructs were made by replacing the TSMod sensor in UNC-70 with an mTFP–Venus FRET pair separated by a 5aa linker or a TRAF domain, respectively[36,37]. Entry clones were made as described above, yielding pENTR TSMod5aa[4 3] and pENTR TSModTRAF[4 3].

Cytoplasmic TSMod (cytoTSMod) was isolated from pENTR TSMod[4 3] using the MK42 primer pair and cloned into pCR Unc70E using the restriction sites SpeI and NsiI. The *unc-70* cDNA coding sequence in pCR Punc-70E was removed by cutting with SpeI and PstI-HF, leaving the *unc-70* promoter and *unc-54* 3′UTR in the backbone.

An N-terminal fusion of TSMod to UNC-70 was made as follows: TSMod was amplified by PCR using primers MK42F and MK43R flanked by SpeI and SalI restriction sites and inserted after the first 15 bp of *unc-70* cDNA under the control of the endogenous *unc-70* promoter. The TSMod and *unc-70* sequences were separated by a flexible linker consisting of five glycines.

Dominant-negative SPC-1 α-spectrin. Single-step PCR with reverse transcription was carried out as described above using primer pair MK42 to amplify a cDNA encoding the first 170 residues of SPC-1 α-spectrin, which contains spectrin domains 0 and 1 (ref. 49). The resulting product was cloned into vector MG115 containing Pmec-17[50] and a C-terminal mCherry tag.

Dynamics of body and neuron curvature. *Image collection.* To image neuron dynamics in moving worms at high resolution (Fig. 1, Fig. 2 and Supplementary Fig. 2, 3), individual *uIs31 [TRN::GFP]* worms were mounted on 1–2% agarose pads, as described[51]. Worms were free to move without crawling out of the field of view, enabling diffraction-limited observation of neuron morphology. Still images and short movies (0.5 fps, about 75 s) were collected at ×20 magnification on a Leica SP5. These movies were analysed post hoc to derive the curvature of both the body and the AVM neuron, neuron length L and neuron strain $\Delta L/L$. At least 17 animals and an average of 6.9 still images were examined for each genotype.

Image analysis. Body curvature was calculated as follows. Using Fiji (ref. 52), the ventral side of the animal was marked with 10–20 individual points between the terminal bulb of the pharynx and the nose. The coordinates were imported into IGOR Pro (Wavemetrics) to calculate curvature according to

$$\frac{x'y'' - y'x''}{\left(x'^2 + y'^2\right)^{\frac{3}{2}}}$$

where x' and x'' are the first and second derivatives of the projection in x; y' and y'' are the first and second derivatives of the projection in y. When the animal bends towards its ventral (dorsal) side, the curvature is positive (negative). Body curvature was used together with a model of body deformation (Supplementary Information) to calculate body strain (Fig. 1c).

Neuron (AVM) curvature was measured by modifying the strategy for body curvature to account for bucking observed during ventral flexures in *unc-70* mutants. The neurite was traced with 20–30 points distributed along a ∼100 μm segment centred at the nerve ring and the curvature at each point was calculated. The mean ± s.d. of these curvatures yielded one data point (Fig. 2b, Supplementary Fig. 3b). The s.d. of the neuron curvature in each frame was calculated as a running average of 20 frames and plotted against body curvature (Fig. 2b, Supplementary Fig. 2b, 3b).

Neuron length, L, was determined by tracing the anterior branch of AVM from the nerve ring to the nose. This path was imported into IGOR Pro and its length and curvature, c, were calculated for several consecutive images in a stack. Neuron length was normalized to yield the effective strain, $(L - L_0)/L_0$, with L as the instantaneous neuron length and L_0 the length at zero curvature, which was determined by fitting a line to the raw data ($L(c) = L_0 + \chi c$) and estimated from the fit parameters according to $L(0) = L_0$. The slope, χ, is a measure of the compliance (inverse of the stress) of the neuron.

Dynamic atomic force spectroscopy. *Primary cell culture.* TRNs were isolated from wild-type (TU2769 *uIs31*) and mutant animals using standard protocols[53] and plated onto peanut lectin-coated glass bottom Petri dishes (WillCo). Mixed cultures of embryonic cells were grown for up to 7 days in L-15 medium supplemented with heat-inactivated fetal calf serum (10% v/v), penicillin (10 mg mL^{-1}), and streptomycin (100 units). Individual TRNs were visualized by their expression of GFP (Fig. 3a).

Atomic force spectroscopy. We used an AFM designed for cell measurements (Bruker BioScope Catalyst, loan from BrukerNano) mounted on a Nikon Eclipse 2000 equipped for epifluorescence to carry out AFM force spectroscopy as described[54]. Cantilevers (Olympus Biolever, 6 mN m^{-1}) were coated overnight with peanut lectin (1 mg/mL) in MES buffer (pH 6.0, 50 mM) and calibrated according to a thermal noise method[55].

Individual TRNs were identified by GFP fluorescence and positioned under a cantilever, which was used to pull membrane nanotubes after 100–900 ms contact time and 400 pN contact force. Interaction frequency was adjusted so that ∼20% of all cell-cantilever contacts yielded a nanotube event, a maneuver that ensures that only single tether events were analysed. Pulling velocity was changed randomly to decrease history effect. No history effect was observed. The number of cells analysed for each genotype and condition is given in Supplementary Table 3. Force-distance curves were analysed using a step fitting algorithm[54]. Mean tether force was plotted against extrusion velocity and fit to a recently proposed model[30] to estimate the static force, f_0, which was used to estimate tension according to $f_0 = 2\pi\sqrt{2\kappa(T_m + W_0)}$ (refs 29,30), where T_m is the in-plane membrane tension and W_0 is the bilayer-cytoskeleton adhesion energy, and κ is the bending rigidity. The bending rigidity was assumed to be 2.7×10^{-19} Nm (ref. 29). Log–log-transformed data was used to carry out linear regression followed by Tukey-type test on multiple regressions to

DOI: 10.1038/ncb2915

assess statistical significance as a function of genotype. Logarithmically transformed data was well fit by a line with slope 1/3 (not shown) as predicted by the power law[30]. The *P* value is shown in Fig. 3 for individual comparisons under the hypothesis that the elevation of the line is the same. Latrunculin A (1 μM) and cytochalasin D (2 μM) were applied to cells, treated TRNs were analysed by dynamic atomic force spectroscopy and compared with data drawn from untreated neurons analysed on the same day.

***In vivo* laser axotomy and analysis of neurite retraction.** Young adult wild type and mutant worms were immobilized in a drug-free manner using a 5% agar pad, as described[51]. All strains used for these experiments (Fig. 4, Supplementary Fig. 4) contained the *uIs31* transgene to drive GFP expression in the TRNs. Immobilized worms were placed on the stage of a laser scanning confocal microscope equipped with two, pulsed Ti::Sa lasers (Prairie Technologies). One laser was used for imaging and the other for axotomy. Both lasers have an average power of 2.7 W (at 860 nm), 190 fs pulse width and a repetition rate of 80 MHz. The ablation laser was tuned to 720 nm and GFP imaging was carried out at 920nm. The energy per pulse of the ablation laser was attenuated to ∼2 nJ and a pulse train of ∼2 ms was delivered into the sample through a 60x, 0.9 NA water immersion objective. To achieve a focused spot at the sample plane, the ablation laser beam was expanded to fill the back aperture of the microscope lens.

To quantify the evolution of the gap-width vs time, kymographs were binarized, denoised and outlined in Fiji. Measurement of the distance of the two neuronal ends from the outlined image was carried out in IGOR Pro. The time evolution of the resulting gap width was fitted to a single exponential as described[33].

***In vivo* FRET imaging and analysis.** *Image collection.* Young adult worms were immobilized without drugs on a 5% agarpad, as described[51] and imaged with a 63x/1.32 oil immersion lens on a confocal microscope equipped with an Ar ion laser and avalanche photodiode detectors coupled to an upright microscope equipped for epifluorescence illumination (Leica SP5 II, Leica DM6000). Donor (mTFP) and acceptor (Venus) fluorophores were activated with the 458nm and 514nm laser lines, respectively and collected with photodiode detectors tuned to 465-500nm and 520-570nm, respectively. Detector collection efficiency and linearity was determined by imaging dilute, homogenous FITC solutions (0.001–10%, in logarithmic increments) and on the basis of this measurement the gain on the donor and acceptor sensors were adjusted to 150% and 100% to equalize detection efficiency $\frac{\varphi_D}{\varphi_A}$. Exact values were determined on the basis of the counts at a given ROI for these settings. Bleed-through factors were determined by imaging transgenic worms with an intact donor (GN495) or acceptor (GN498) fluorophore during each imaging session and were 0.37 ± 0.05 for the donor channel and 0.17 ± 0.07 for the acceptor channel.

Three image types were collected for each neurite: 1) acceptor excitation-acceptor emission (I_A); 2) donor excitation-donor emission (I_D); 3) donor excitation-acceptor emission (I_F). Portions of the ALM and PLM neurites were identified for imaging on the basis of animal orientation and morphology; other neuronal ROIs included neurites arranged parallel to the long axis of the worm's body.

Image analysis and estimation of FRET efficiency by sensitized emission. For each micrograph, intensity profiles were computed across the diameter of the neurite of interest and fit by a Gaussian to estimate the background intensity, neurite width, and centerline position. The latter information (width, centerline) was used to determine the relevant ROI for subsequent processing. This process was applied to all images to yield the data required to estimate FRET efficiency by sensitized emission following a linear correction for spectral bleed-through. The FRET efficiency, *E* was computed on a pixel-by-pixel basis according to:

$$E = 100\frac{\left(cF\ Q_D \frac{\psi_D}{\psi_A}\right)}{qD + \left(cF\ Q_D \frac{\psi_D}{\psi_A}\right)}$$

where, *cF* and *qD* are the bleedthrough-corrected values for the FRET and donor channels, respectively, Q_D is the quantum yield of the donor chromophore[37], and ψ_D/ψ_A is the ratio of the collection efficiencies of the donor and acceptor emission sensors. The uncertainty of each pixel was estimated as described[56] and pixels with errors >500% were rejected from analysis; the remaining pixels were averaged to yield an average *E* for each ROI.

To better understand the accuracy of this sensitized emission technique, we also carried out FLIM on the same transgenic animals as described[37]. Briefly, worms were immobilized as described and imaged with an SP5 confocal system equipped with a Becker&Hickl SPC-150 module for time-correlated photon counting. Photons were accumulated for up to 150 frames (3 minutes) using a ×20 oil immersion lens and <5% transmission of a pulsed Ti::Sa laser at 870 nm through a 475/28nm emission bandpass filter. Fluorescence lifetime histogram was fitted using a double-exponential decay function, convolved with a synthetic IRF, to extract the amplitude weighted mean of the two components of the excited state lifetime. The lifetime of the donor by itself (in absence of the acceptor) was measured using mTFP transfected MDCK cells. FRET efficiency was calculated according to $E = 1 - \frac{\tau_{DA}}{\tau_{DD}}$ in which τ_{DA} is the lifetime of the donor in presence of the acceptor and τ_{DD} is the lifetime of the donor alone. These independent estimates of FRET efficiency yielded essentially identical values for all TSMod isoforms tested (Supplementary Fig. 6). Moreover, FRET efficiency values for the low FRET (TRAF) and high FRET (5aa) UNC-70 isoforms are similar to published values derived from *in vitro* measurements of mTFP-TRAF-Venus and mTFP-5aa-Venus[36].

FRET imaging following laser axotomy Transgenic animals expressing UNC-70(TSMod) and UNC-70(TRAF) were immobilized on the stage of the Leica SP5 imaging station and TRNs were axotomized with a pulsed Ti::Sa laser (2.7 W, 860 nm) using 70% transmission and were ablated by scanning over a 1024×32 pixel ROI for 200 ms and left to retract for ∼5 s before imaging the proximal end, as described above. A final image was taken to calculate FRET after cutting.

Fluorescence recovery after photobleaching (FRAP). Transgenic animals were immobilized on agarose pads, as described[51] and placed on the stage of confocal microscope. UNC-70(TSMod) was analysed with a Leica SP5 II and a 63x/1.3 oil immersion lens. Under the control of FRAP Wizard software, a short segment (2–4 μm long) of a TSMod-expressing neurite was illuminated at full power for 1.5 s at 458nm and 514 nm. The same region of interest (ROI) was subsequently imaged for 10 frames at 0.6 fps and 20 frames at 0.1 fps, exciting the Venus fluorophore. This system lacked the temporal resolution needed to analyse rapid recovery of cytosplasmic cytoTSMod. Therefore, a Prairie Technologies dual 2-photon microscope was used to image and bleach the neurite of cytoTSMod simultaneously using 920nm excitation with a 60x/0.9 water immersion lens. A line scan of ∼10–20 μm in length was imaged at 1000 fps for 1s to image the recovery process. Image stacks were analysed to plot intensity versus time and used to derive *D*, the effective diffusion constant.

Immunofluorescence. Animals were fixed and subjected to antibody labeling as described[4]. Fixed animals were treated with anti-myotactin antibodies (MH46, Developmental Studies Hybridoma Bank) at 1:50 dilution in B-PBST (PBS + 0.1% Triton-X100 + 3% BSA), incubated overnight at 4 °C, and washed several times in B-PBST. Next, samples were treated with an anti-mouse secondary antibody (Alexa567-tagged, 1:2000, LifeTechnologies) overnight, washed in B-PBST, and mounted in VectorShield, cured for several hours (4 °C), and imaged in a Leica SP5 confocal system. Interpunctum interval (IPI) was determined from intensity profiles, as described[58]. The binsize for IPI histograms was calculated according to Freedman-Diaconis rule: $width = 3.49N^{0.3}$, where *N* is the number of observations. Histograms were normalized to yield a probability density function, which were fitted by a Gamma-distribution.

Statistical and computational analysis. Unless indicated, computations and statistical analyses were carried out using IGOR Pro 6.04 (Wavemetrics) and image analysis was carried out with NIH ImageJ or Fiji software[52].

48. Stiernagle, T.Maintenance of C. elegans (February 11, 2006), *WormBook*, ed. The C. elegans Research Community, WormBook, http://dx.doi.org/10.1895/wormbook.1.101.1 .
49. Norman, K. R. & Moerman, D. G. Alpha spectrin is essential for morphogenesis and body wall muscle formation in *Caenorhabditis elegans*. *J. Cell Biol.* **157,** 665–677 (2002).
50. Shida, T., Cueva, J. G., Xu, Z., Goodman, M. B. & Nachury, M. V. The major α-tubulin K40 acetyltransferase αTAT1 promotes rapid ciliogenesis and efficient mechanosensation. *Proc. Nat. Acad. Sci. USA* **107,** 21517–21522 (2010).
51. Kim, E., Sun, L., Gabel, C. V. & Fang-Yen, C. Long-term imaging of *Caenorhabditis elegans* using nanoparticle-mediated immobilization. *PloS One* **8,** e53419 (2013).
52. Schindelin, J. *et al.* Fiji: an open-source platform for biological-image analysis. *Nat. Methods* **9,** 676–682 (2012).
53. Strange, K., Christensen, M. & Morrison, R. Primary culture of *Caenorhabditis elegans* developing embryo cells for electrophysiological, cell biological and molecular studies. *Nat. Protocols* **2,** 1003–1012 (2007).
54. Krieg, M., Helenius, J., Heisenberg, C.-P. & Müller, D. J. A bond for a lifetime: employing membrane nanotubes from living cells to determine receptor-ligand kinetics. *Angew. Chem.* **47,** 9775–9777 (2008).
55. Hutter, J. L. & Bechhoefer, J. Calibration of Atomic-Force Microscope Tips (Vol 64, 1868, 1993). *Rev. Sci. Instrum.* **64,** 3342–3342 (1993).
56. Zar, J. H.*Biostatistical analysis* (Pearson College Div, 2010).
57. Sprague, B. L., Pego, R. L., Stavreva, D. A. & McNally, J. G. Analysis of Binding Reactions by Fluorescence Recovery after Photobleaching. *Biophys. J.* **86,** 3473–3495 (2004).
58. Árnadóttir, J., O'Hagan, R., Chen, Y., Goodman, M. B. & Chalfie, M. The DEG/ENaC protein MEC-10 regulates the transduction channel complex in *Caenorhabditis elegans* touch receptor neurons. *J. Neurosci.* **31,** 12695–12704 (2011).

DOI: 10.1038/ncb2915

nature cell biology

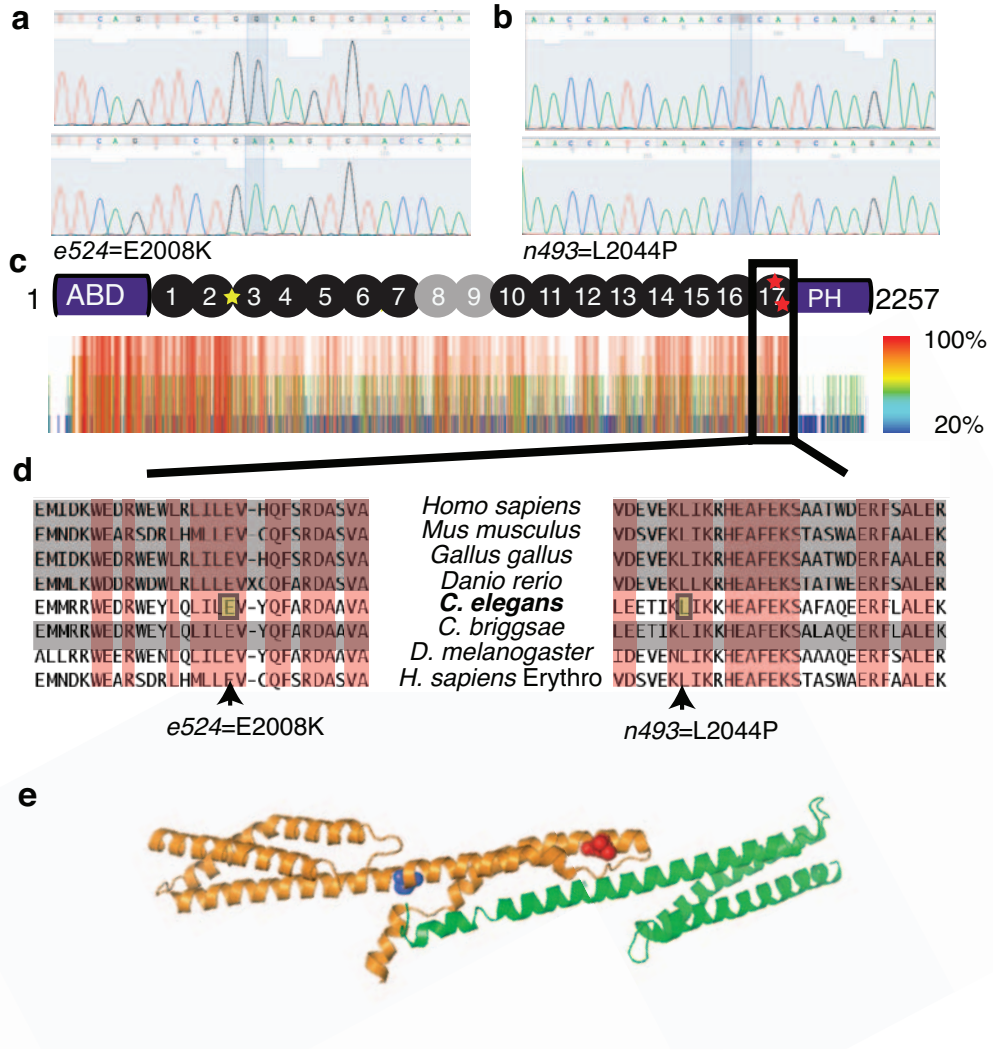

Supplementary Figure 1 *unc-70(e524)* and *unc-70(n493)* encode missense mutations of conserved residues in UNC-70 β-spectrin. **a,** Chromatogram of the *unc-70* locus in wild type (top) and *unc-70* mutant (bottom) worms near the codon encoding E2008. **b,** Chromatogram of the *unc-70* locus in wild type (top) and *unc-70* mutant (bottom) worms the codon encoding L2044P. **c,** Schematic domain architecture of *C. elegans* UNC-70 β–spectrin, consisting of an N-terminal actin binding domain (ABD), 17 spectrin repeats and a C-terminal PH domain. Yellow star indicates the position of the premature stop codon encoded by *unc-70(s1502)*; red stars show the position of the missense mutations encoded by *unc-70(n493)* and *unc-70(e524)*. Protein sequence alignment of human erythrocyte β-spectrin and non-erythrocyte β-spectrin from seven species: *Homo sapiens*, *Mus musculus*, *Gallus gallus*, *Danio rerio*, *C. elegans*, *C. briggsae*, *D. melanogaster*. Color scale represents the degree of conservation; red=100% and blue=20%. **d,** Close-up view of the sequence alignment of spectrin repeat 17. Highlighted in red are residues that are 100% conserved in all species; green boxes are the two missense mutations used in this study. **e,** 3-D model of the α-β tetramerization domain. Orange indicates β-spectrin repeats R16 and R17; green indicates α-spectrin repeats R0 and R1. The two mutated residues, E2008K in *unc-70(e524)* and L2044P in *unc-70(n493)* are shown in space-filling mode. Figure assembled in PyMol from PDB 3LBX (Ref. 1).

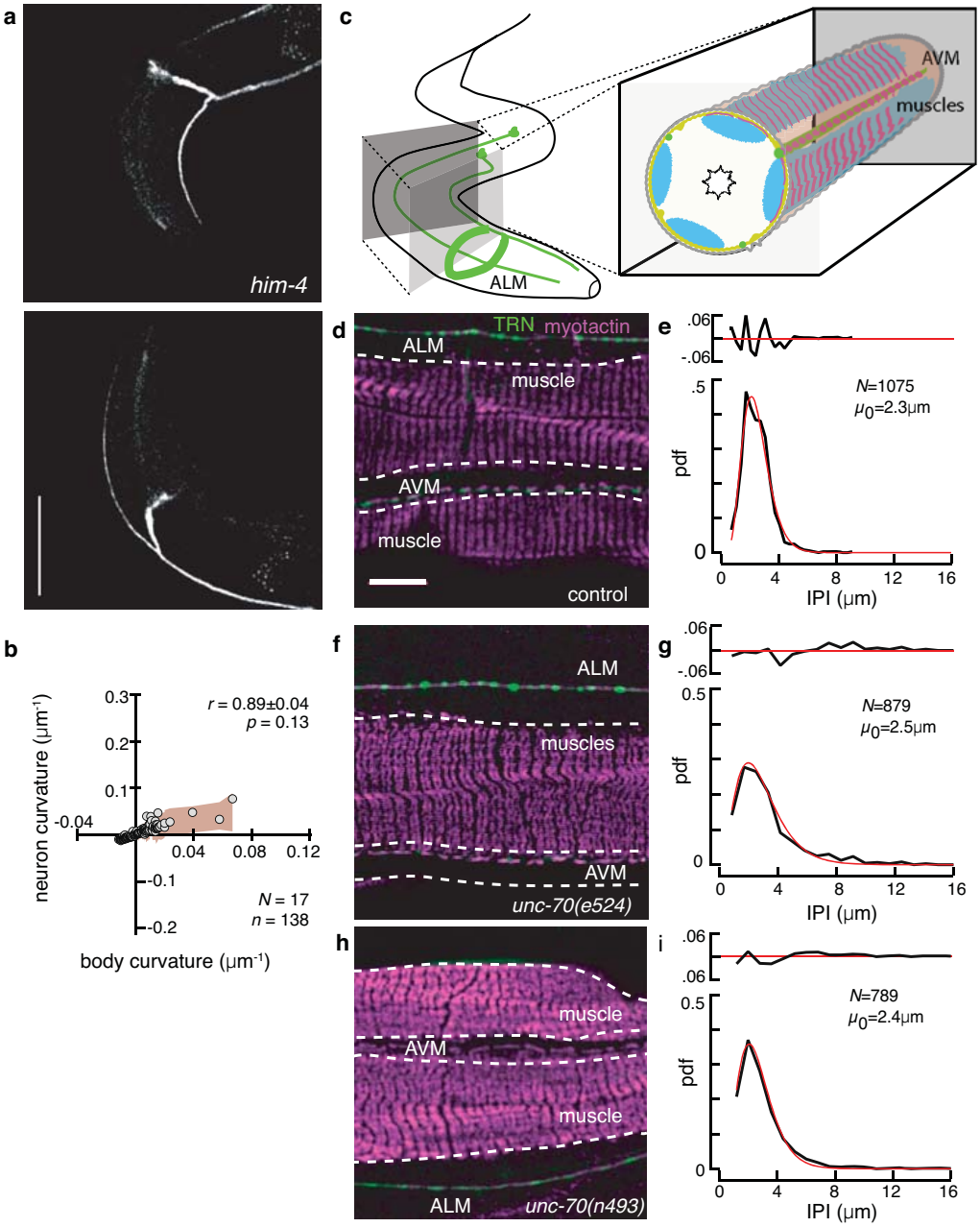

Supplementary Figure 2 Disrupting the TRN-epidermis attachment is not sufficient to cause buckling and attachments are intact in *unc-70* mutants. **a,** AVM shape during dorsal (top) and ventral (bottom) bending in *him-4(e1267)* mutants lacking full hypodermal attachment. **b,** Neuron curvature vs. body curvature in *him-4(e1267)* mutants. *N* = number of animals and *n* = number of still images; collected during *n*=4 imaging sessions. **c,** UNC-70 is not required for TRN attachment. **(c)** Schematic showing the position of the ALML and AVM. The slab visualizes the arrangement of muscles (blue) and TRNs (green) in respect to the body axis. Individual attachment sites linking body wall muscles and TRNs to the hypodermis are shown in magenta. **d,f,h,** Representative micrographs anti-myotactin showing attachment sites in **(d)** control, **(f)** *unc-70(e524)* and (h) *unc-70(n493)* mutant animals. **e,g,i,** Distribution of interpunctum intervals for attachment sites stained in **(e)** control, **(g)** *unc-70(e524)* and **(i)** *unc-70(n493)*. Distributions were fit to a Gamma-distribution with the median location and the residuals from each fit are shown above each graph. *N* = number of interpunctum intervals analyzed for each genotype; more than 25 images analyzed for each genotype during *n*=3 imaging sessions.

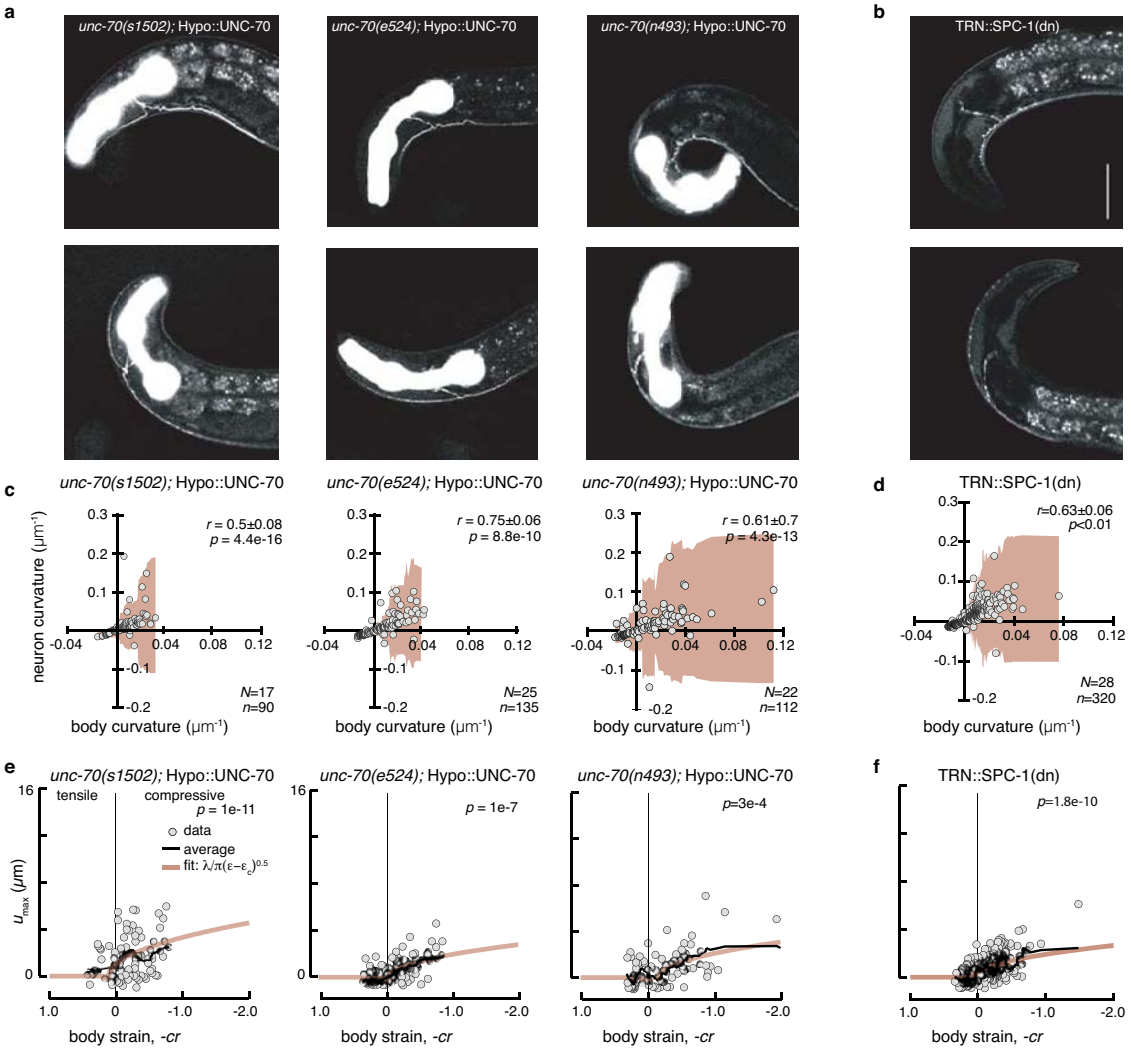

Supplementary Figure 3 Expressing wild-type UNC-70 in the epidermis reduces buckling observed in *unc-70* mutants. **a,** Representative images of AVM shape during ventral (top) and dorsal (bottom) bending in *unc-70(s1502);oxIs95*, *unc-70(e524);oxIs95*, *unc-70(n493);oxIs95* mutant animals. The *oxIs95* transgene drives expression of full-length, wild-type UNC-70 in the epidermis. The bright fluorescence in the pharynx is the co-transformation marker used to construct transgenic animals expressing wild-type *unc-70* in the epidermis **b,** AVM shape during ventral (top) and dorsal (bottom) bending in transgenic worms expressing a dominant negative α-spectrin fragment in TRNs only. Scale bar in b applies to a and is 50 µm. **c,** Average neuron curvature *vs.* average body curvature of the same genotypes as in a. Each point is an average of 10-30 curvature measurements along the body in each frame (see Methods). The shaded area (beige) is a moving average of the standard deviation for 15-20 points. *r* is the Pearson's correlation coefficient of neuron and body curvature. Statistical difference of the correlation coefficient *r* was tested using a Fisher z-transform of *r*; *p* values relative to controls are indicated in the upper right. *n* still images collected from *N* animals during three imaging sessions. **d,** Average neuron curvature *vs.* average body curvature of the same genotypes as in b. Each point is an average of 10-30 curvature measurements along the body in each frame (see Methods). The shaded area (beige) is a moving average of the standard deviation for 15-20 points. *r* is the Pearson's correlation coefficient of neuron and body curvature. Statistical difference of the correlation coefficient *r* was tested using a Fisher z-transform of *r*. Significant differences to control worms are indicated by a *p* value indicated in the upper right. *n* still images collected from *N* animals during three imaging sessions. **e, f,** Maximum off-axis deformation (buckling), u_{max}, of AVM as a function of body strain derived from the data in c and d. Each point is the maximum deformation detected at a given body posture. Solid black line is a running average of 15 images; beige curve is a fit of the buckling deformation as function of ε (see Supplementary Note 1). Exact *p* values (upper left) are relative to wild type, with a significance level of α=0.01. Tensile strain is positive and increases to the left, compressive strain is negative and increases to the right of the zero strain.

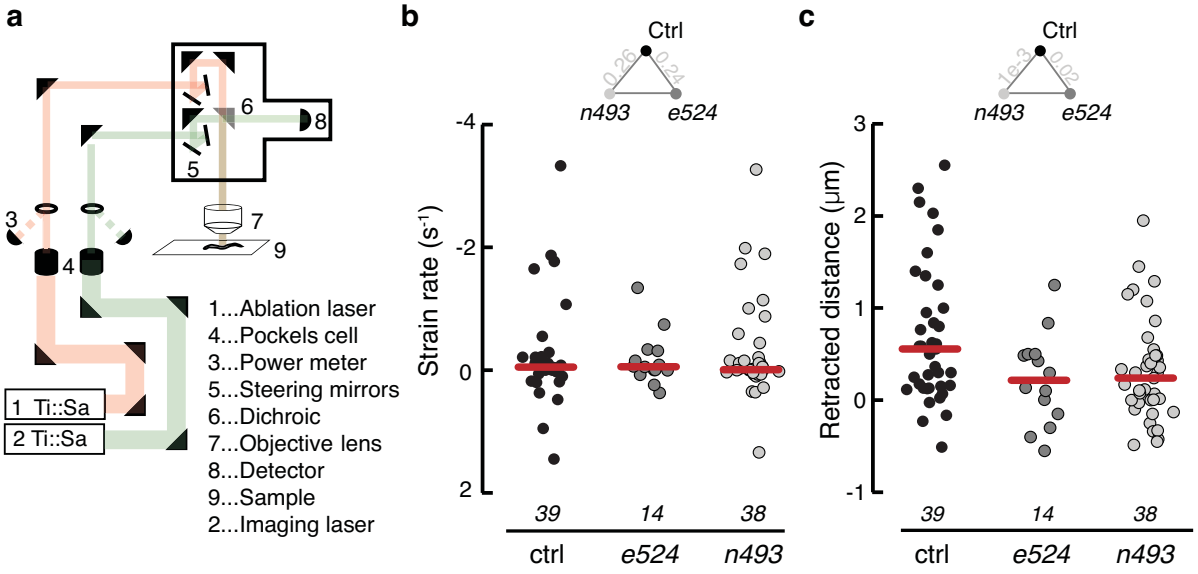

Supplementary Figure 4 Laser axotomy of TRNs in *him-4(+)* worms. **a,** Schematic of the dual-femtosecond laser axotomy set-up. **b,** Strain rate of control and *unc-70* mutant TRNs after laser cutting. Thick horizontal bars are the median and the number of axotomies is indicated in each column. Axotomies were performed in *n*=16 control, *n*=5 *unc-70(e524)*, and *n*=7 *unc-70(n493)* animals during four imaging sessions/genotype. Negative values occur either due to relaxation of an initially compressed neurite, relaxation after initial expansion during ablation or diffusion of fluorophore into the initially bleached ends proximal to the cut site. Median values were significantly different (U-test); *p* values (inset) show no significant difference as a function of genotype. **c,** Retracted distance, $D_0/2$, in control and *unc-70* mutant worms after laser cutting. Bars are the median retracted distance for and *p*-values derived from a U-test are shown in the inset.

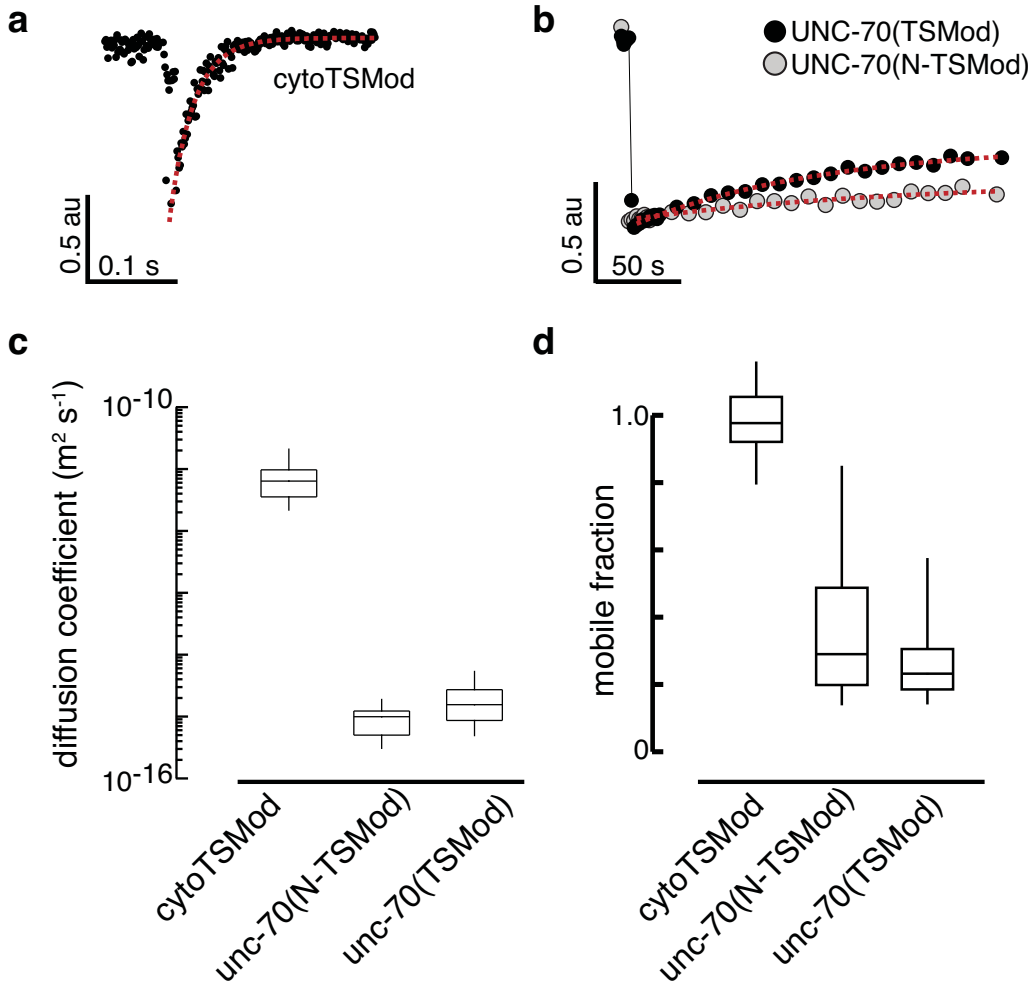

Supplementary Figure 5 UNC-70(TSMod) and UNC-70(N-TSMod) are less mobile that cytoTSMod. **a,** Representative fluorescence recovery after photobleaching (FRAP) trace for cytoplasmic TSMod. Red curve is a single exponential fit to the data points. Similar results obtained in *n*=17 neurites analyzed during two imaging sessions. Note, recovery was complete after bleaching. **b,** Representative FRAP traces of UNC-70(TSMod) and UNC-70(N-TSMod). Red curves are exponential fits to the data. Similar results were obtained in n=13 neurites for both UNC-70(TSMod) and UNC-70(N-TSMod) analyzed during two imaging sessions. **c,** Diffusion coefficients estimated from rate of fluorescence recovery for UNC-70(TSMod), N-TSMod, and cytoTSMod. Box plots show the median, quartiles and 0.1 and 0.9 percentiles. **d,** Mobile fraction of UNC-70(TSMod), N-TSMod and cytoTSMod expressing neurites. Box plots show the median, quartiles and 0.1 and 0.9 percentiles.

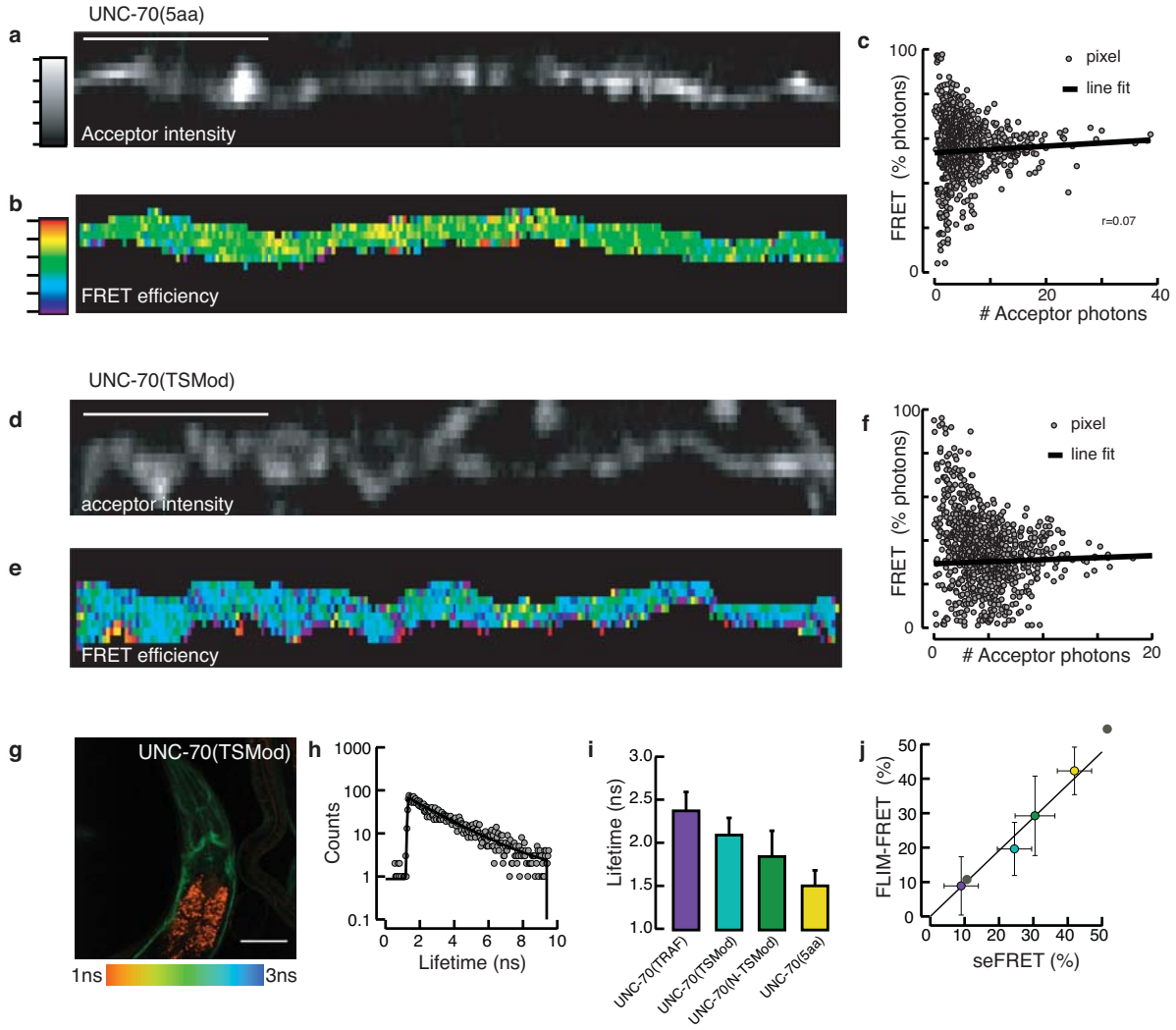

Supplementary Figure 6 Intermolecular FRET assessment and fluorescence lifetime measurements. **a, b,** Number of photons emitted by UNC-70(5aa)/High FRET worms in the (a) acceptor channel after direct illumination and (b) the corresponding FRET efficiency image based in the number of photons collected for each bleed-through corrected pixel. c Distribution of photons undergoing FRET (FRET efficiency) after donor excitation *vs.* number of acceptor photon after direct excitation of the acceptor. Each dot indicates a measurement derived from a pixel in (b). Black line is a linear fit to the 200 points with the highest acceptor photon counts. *r* is the correlation coefficient of the fit. d-f Same representation as above for UNC-70(TSMod) worms. **g,** Representative fluorescence lifetime image (FLIM) of a UNC-70(TSMod) expressing worm. Lookup table corresponds to the fluorescence lifetime at each pixel derived from the photon arrival histogram after fitting with a double exponential decay. Similar images were obtained in more than 6 animals. **h,** Fluorescence lifetime histogram of a representative pixel showing the number of photons collected as a function of arrival time. Black solid line indicates a double exponential fit to the data convolved with a synthetic instrument response function. **i,** Fluorescence lifetime for nine ROIs in *n*=6 worms analyzed during two imaging sessions. **j,** Correlation between FLIM-FRET efficiency and sensitized emission FRET efficiency derived from intensity based measurements (mean±SD). Black solid line indicates perfect correlation of the two quantities. Gray dots are values taken from published studies of constructs using the same genetically-encoded flurophores[2, 3]. High and low FRET values were taken from Day, et al. (Ref. 3).

Supplementary Table Legends

Supplementary Table 1 *C. elegans* strains and transgenes. List of all of the *C. elegans* strains used or created for this study and all of the transgenes created for this study.

Supplementary Table 2 Primers used to build novel transgenes. Lists the purpose and sequence of PCR primers used in this study.

Supplementary Table 3 Number of tethers analyzed by AFM force spectroscopy as a function of genotype, velocity, and treatment condition.

Supplementary Video Legends

Supplementary Video 1 Control worm expressing GFP in touch receptor neurons. Movie shows AVM morphology during ventral (compressive) and dorsal (tensile) bending. Scale bar: 50μm. Frame rate: 0.5/s.

Supplementary Video 2 *unc-70(s1502)* mutant worm expressing GFP in touch receptor neurons. Movie shows AVM morphology during ventral (compressive) and dorsal (tensile) bending. Scale bar: 50μm. Frame rate: 0.5/s.

Supplementary Video 3 *unc-70(e524)* mutant worm expressing GFP in touch receptor neurons. Movie shows AVM morphology during ventral (compressive) and dorsal (tensile) bending. Scale bar: 50μm. Frame rate: 0.5/s.

Supplementary Video 4 *unc-70(n493)* mutant worm expressing GFP in touch receptor neurons. Movie shows AVM morphology during ventral (compressive) and dorsal (tensile) bending. Scale bar: 50μm. Frame rate: 0.5/s.

Supplementary Note

This note describes how we analyzed neuronal buckling *in vivo*; this model relates to the data and analyses shown in Fig. 1, 2 and Supplementary Fig. 3. The goal of this analysis was two-fold. First, we sought to quantify AVM buckling as a function of body strain. Second, we applied a simple phenomenological mechanical model to characterize the relationship between neuron buckling and body bending as function of genotype. AVM buckling was measured in these three steps: 1) an ROI containing the neuron of interest was selected and straightened in ImageJ; 2) the image of the straightened neuron was converted to a binary image, denoised and thinned to a 1-pixel skeleton; 3) the maximum off-axis distance in each frame, u_{max}, was determined by computing the least-squared-minimized difference between each pixel in the skeleton and a straight line fit to the data. To derive body strain, we treated the worm's body as an elastic Euler-Bernoulli tube and derived strain from stress according to $\varepsilon = -r\,c$ with r as the distance of the neuron from the neutral axis (worm radius at the nerve ring) and c the curvature of the worm's body. The results of this analysis are plotted in Fig. 2c and Supplementary Fig. 3e, f.

Deformation modeling and assumptions

To interpret these data, we took advantage of a model from continuum mechanics of a slender rod embedded in an elastic matrix. To apply the model, we harness the wealth of the detailed information about the ultrastructure and morphology of TRNs and their environment. For example the TRNs are filled with bundles of cross linked microtubules[4, 5] and we assumed that this long structure behaves like a slender rod embedded in an elastic matrix subjected to compressive forces during body bending.

The TRN microtubule bundle is embedded into a visco-elastic cytoplasm surrounded by other cytoskeletal elements. In turn, the neuron is embedded in surrounding tissues within the body of the living animal, imposing physical constraints. In the context of the model, it does not matter whether the dominant elastic elements are within the neuron or surround the neuron. Therefore, we combined all these elements (cytoplasm, neuronal membrane, hypodermis) together and modeled them as a continuum elastic matrix.

In principle, the bending and buckling dynamics of microtubules can be used to probe properties of the local environment of the microtubule[6]. Here we use an approach that incorporates current knowledge about the neuronal microtubule cytoskeleton to make qualitative inferences about the changes in the mechanical properties of the elastic matrix.

Buckling

We modeled a microtubule bundle embedded in an elastic matrix that undergoes oscillatory buckling undulations with a wavelength λ when the compressive strain exceeds a critical threshold[6, 7]. The wavelength, λ, depends only on the overall bending rigidity of the bundle, κ_B, and on the elasticity, E_m, of the surrounding matrix according to

$$\lambda \approx \frac{4}{3}\left(\frac{\kappa_B(1-\nu^2)}{E_m}\right)^{\frac{1}{4}} \quad (1)$$

with κ_B as the flexural rigidity of the microtubule bundle, ν as the Poisson ratio and E_m as the effective Young's modulus of the constraining matrix[8].

Therefore, it should be possible to use well-characterized microtubule mechanics to estimate the relative differences between effective elasticities from measurements of λ.

Beyond critical threshold the maximum amplitude u_{max} of the `buckling wave' scales as the square-root of the axial compressive strain according to as:

$$u_{\max}(\varepsilon) = \frac{\lambda}{\pi}\sqrt{(\varepsilon - \varepsilon_c)} \quad (2)$$

where, ε_c is the critical strain and ε is the compressive strain[8, 9]. To fit this equation to the data in Fig. 2c and Supplementary Fig 3c,d, we multiplied body strain ε by -1. This equation was fit to plots of u_{max} *vs.* body strain above the approximate ε_c to derive λ (Fig. 2c, Supplementary Fig. 3c, 3d). Similar to λ, ε_c provides insight into the elasticity of the constraining matrix and represents the range of compressive strains over which the rod remains stable. Both the elasticity of the surrounding matrix and pre-tension within the rod can contribute to ε_c (Ref. 6, 8, 10).

Model discussion and assumptions

The buckling filament is stabilized by a linear, isotropic matrix.

Strain and stress during body bending is assumed to be linear, leading to a linearly increasing axial compression force due to the bending moment imposed by muscle contraction. Previous measurements using piezoresistive cantilevers suggests that worms show a linear elasticity at the deformations tested[14]. Because both the neuron and the surrounding hypodermal cell assemble a spectrin network, it is likely that cell-autonomous and cell-nonautonomous factors contribute to the stabilization. This conclusion is supported by data in Supplementary Fig. 3, in which the manipulation of the spectrin network in the hypodermis as well as in the TRNs modulates the buckling behavior.

The neuron deformation is not caused by buckling of the cuticle

Buckling of the cuticle is, likely to play a role at very high body bending, creating strains of more than 100% as seen for *unc-70* mutants in Fig. 2c, and

Supplementary Fig 3. In such a situation, the data deviates from the theoretically predicted buckling behavior and off-axis deformations increase

$$u_{\max}(\varepsilon) >> \frac{\lambda}{\pi}\sqrt{\varepsilon - \varepsilon_c} \tag{3}$$

In general, we do not observe cuticle buckling at the lower strains that commonly occur during locomotion.

Neuron bending is approximated by the flexural rigidity of the microtubule bundle inside the TRNs

To relate the wavelength λ derived from the fit of Equation 2 to an actual elasticity (Equation 1), we need to make assumptions about the bending elasticity of the microtubule bundle. For the limiting case of a completely uncoupled bundle of microtubules, the flexural rigidity increases linearly with the number of individual microtubules inside the bundle[15] according to: $\kappa_B = N \cdot \kappa_{MT}$. Due to the uncertainty on the behavior of the microtubule bundle, exact absolute values for E_m cannot be extracted from the model. Electron micrographs show that adult TRNs contain an average of N=60 microtubules[5]. If we assume a flexural rigidity of κ_{MT} = 2-7×10^{-23} N m^2 for an individual microtubule[13, 16], then we derive an elasticity for wild type worms of $E_m \approx 10^6$ Pa, surprisingly close to values for elasticity of worm body reported in the literature[14, 17].

Neuronal microtubules undergo buckling in living cells

Buckling of microtubules has been observed *in vitro*[11], in living cells[6] and in organisms[12]. Microtubules are by orders of magnitude the stiffest components inside living cells[13]. Given microtubules relative incompressibility, buckling remains an energetically favorable way to reduce length under axially applied forces[7].

Supplementary References

1. Ipsaro, J.J. *et al.* Crystal structure and functional interpretation of the erythrocyte spectrin tetramerization domain complex. *Blood* **115**, 4843-4852 (2010).
2. Borghi, N. *et al.* E-cadherin is under constitutive actomyosin-generated tension that is increased at cell-cell contacts upon externally applied stretch. *Proceedings of the National Academy of Sciences of the United States of America* **109**, 12568-12573 (2012).
3. Day, R.N., Booker, C.F. & Periasamy, A. Characterization of an improved donor fluorescent protein for Forster resonance energy transfer microscopy. *Journal of biomedical optics* **13**, 031203 (2008).
4. Chalfie, M. & Thomson, J.N. Structural and functional diversity in the neuronal microtubules of Caenorhabditis elegans. *The Journal of Cell Biology* **93**, 15-23 (1982).
5. Cueva, J.G., Mulholland, A. & Goodman, M.B. Nanoscale organization of the MEC-4 DEG/ENaC sensory mechanotransduction channel in Caenorhabditis elegans touch receptor neurons. *Journal of Neuroscience* **27**, 14089-14098 (2007).
6. Brangwynne, C.P. *et al.* Microtubules can bear enhanced compressive loads in living cells because of lateral reinforcement. *The Journal of Cell Biology* **173**, 733-741 (2006).
7. Landau, L.D., Pitaevskii, L.P., Lifshitz, E.M. & Kosevich, A.M. *Theory of Elasticity, Third Edition: Volume 7 (Theoretical Physics)*. (Butterworth-Heinemann, 1986).
8. Xiao, J. *et al.* Mechanics of buckled carbon nanotubes on elastomeric substrates. *Journal of Applied Physics* **104**, 033543 (2008).
9. Jiang, H. & Zhang, J. Mechanics of Microtubule Buckling Supported by Cytoplasm. *Journal of Applied Mechanics* **75**, 061019 (2008).
10. Das, M., Levine, A.J. & MacKintosh, F.C. Buckling and force propagation along intracellular microtubules. *Epl* **84** (2008).
11. Kurachi, M., Hoshi, M. & Tashiro, H. Buckling of a single microtubule by optical trapping forces: direct measurement of microtubule rigidity. *Cell Motility and the Cytoskeleton* **30**, 221-228 (1995).
12. Topalidou, I. *et al.* Genetically Separable Functions of the MEC-17 Tubulin Acetyltransferase Affect Microtubule Organization. *Current Biology*, 1-9 (2012).
13. Gittes, F., Mickey, B., Nettleton, J. & Howard, J. Flexural rigidity of microtubules and actin filaments measured from thermal fluctuations in shape. *The Journal of Cell Biology* **120**, 923-934 (1993).
14. Park, S.-J., Goodman, M.B. & Pruitt, B.L. Analysis of nematode mechanics by piezoresistive displacement clamp. *Proceedings of the National*

Academy of Sciences of the United States of America **104**, 17376-17381 (2007).
15. Guo, Y., Liu, Y., Tang, J.X. & Valles, J.M. Polymerization force driven buckling of microtubule bundles determines the wavelength of patterns formed in tubulin solutions. *Physical review letters* **98**, 198103 (2007).
16. Tolomeo, J.A. & Holley, M.C. Mechanics of microtubule bundles in pillar cells from the inner ear. *Biophysical Journal* **73**, 2241-2247 (1997).
17. Fang-Yen, C. *et al.* Biomechanical analysis of gait adaptation in the nematode Caenorhabditis elegans. *Proceedings of the National Academy of Sciences of the United States of America* **107**, 20323-20328 (2010).